Eigen-frequencies and harmonic responses in topology optimisation: A CAD-compatible algorithm

Giulio Costa, Marco Montemurro

To cite this version:

Giulio Costa, Marco Montemurro. Eigen-frequencies and harmonic responses in topology optimisation: A CAD-compatible algorithm. Engineering Structures, 2020, 214, pp.1-24. 10.1016/j.engstruct.2020.110602 . hal-03166964

HAL Id: hal-03166964
https://hal.inrae.fr/hal-03166964v1

Submitted on 22 Aug 2022

Eigen-frequencies and harmonic responses in topology optimisation: a CAD-compatible algorithm

Giulio Costa[a,b], Marco Montemurro[a,1]

[a] *Arts et Métiers Institute of Technology, Université de Bordeaux, CNRS, INRA, Bordeaux INP, HESAM Université, I2M UMR 5295, F-33405 Talence, France*
[b] *EPSILON - Groupe ALCEN, Site ENSAM, Esplanade d'Arts et Métiers 33405 Talence, France*

Abstract

The formulation of Topology Optimisation (TO) problems related to dynamics is particularly challenging, due to some intrinsic difficulties of mathematical and numerical nature. This paper deals with the integration of specific physical quantities, such as eigen-frequencies and dynamic compliance, in a special TO algorithm, which combines a classical pseudo-density field with Non-Uniform Rational Basis Spline (NURBS) entities. In this framework, wherein some of the NURBS continuous parameters (i.e. control points and weights) are the new design variables, important advantages can be exploited. In particular, beyond the reduction of the number of design variables and the definition of an implicit filter zones, the post-processing phase involving the CAD reconstruction of the optimised geometry is immediate for 2D problems and needs few operations in 3D. Classical TO problems dealing with structural dynamics, as the maximisation of the first eigen-frequency and the minimisation of the dynamic compliance, are formulated in the NURBS framework. Accordingly, the analytical expressions of the gradients of the considered physical quantities are derived in closed form. In order to show the effectiveness of the proposed approach, an exhaustive numerical campaign is proposed and the algorithm is applied to both 2D and 3D benchmarks. Moreover, a sensitivity analysis of the final optimised solutions to the NURBS discrete parameters is provided as well.

Email address: `marco.montemurro@ensam.eu; marco.montemurro@u-bordeaux.fr` (Marco Montemurro)

[1] Corresponding author

Preprint submitted to Engineering Structures *March 21, 2020*

Keywords: Topology Optimisation, NURBS, SIMP, Dynamics, Eigen-frequencies, Harmonic Loads

---

1. Introduction

Topology Optimisation (TO) identifies a specific class of optimisation algorithms, wherein the aim is to find the optimal material lay-out in a prescribed design domain. The material is distributed in order to minimise an objective/cost function by satisfying some additional requirements. Pioneering TO algorithms made use of the homogenisation technique [1]. Nowadays, TO analyses are carried out mainly through three well-established families of methods: density-based methods [2], Level-Set Methods (LSMs) [3, 4] and the so called Evolutionary Structural Optimisation (ESO) [5]. Regardless of the specific algorithm, the mostly tackled problem in bibliography is the minimisation of the compliance of a structure subject to an equality constraint on the volume. However, practitioners and academics soon started considering other physical responses, in order to fully exploit the potential of TO in design [6].

TO problems dealing with structural dynamics are often addressed because of their prime importance in the design of structures. Particularly, in the last decades, eigen-frequencies and harmonic responses have been integrated in TO algorithms. Dealing with these quantities in TO is a real challenge because some issues of numerical nature arise and they can affect the result even in the simplest case, where non-linearity is neglected.

Handling natural frequencies in structural optimisation presents several common features to linear buckling problems [2, 7]. In TO, the so-called "mode switch" often occurs: since the topology is not set *a priori*, the most critical mode (i.e. that related to the first eigen-value) can change during the optimisation. If the problem at hand involves the maximisation of the first eigen-frequency or the maximisation of the gap between two consecutive eigen-frequencies [8], the mode switch causes a jump in the evaluation of the objective function and of its gradient, with detrimental effects on convergence. Some techniques are available in the literature to circumvent this phenomenon. For instance, a suitable bound-formulation is proposed in [9]. The idea of a weighted mean eigen-frequency is suggested in [10]: rather than maximising the first eigen-frequency, a weighted mean eigen-frequency (involving several modes) is maximised. Among these two techniques, the bound-formulation has been proven to be very useful and efficient [2], whereas the mean eigen-frequency could be more sensitive to the choice of the weights. Other more sophisticated strategies to improve the algorithm robustness consist of a sensitivity analysis provided through the mathematical perturbations technique [11, 12] or the Modal Assurance Criterion [13], which measures the correlation between two modes and assures a good control on the shape of the considered eigen-modes.

An issue of different nature can affect density-based methods and all those LSMs that make use of a "weak" material phase to evaluate dynamic responses. In low-density regions, the penalisation on the stiffness matrix is stronger than the penalisation on the mass matrix and this fact results in spurious/slack vibrating modes. They are characterised by an extremely low eigen-frequency and a localised displacement field. In density-based approaches, increasing the lower bound of the pseudo-density is a common practice to avoid spurious localised modes [14], but this fact invalidates the original TO problem, which becomes a *reinforcement problem*. To avoid this shortcoming, different penalisation schemes for the stiffness matrix can be used (polynomial, piece-wise differentiable functions, etc.), assuring a finite ratio between structural mass and structural stiffness in low density elements [12, 15, 16]. In the framework of LSMs, a particular body-fitted meshing strategy is used in [17] to avoid the weak material phase and only fully dense material properties are assigned to the Finite Element (FE) model.

The mutual penalisation scheme of stiffness and mass matrices plays a fundamental role in any dynamic problem in TO, including those involving the steady state response of a structure subject to a time-harmonic load [18]. A typical problem in TO deals with the minimisation of a global dynamic response and several objective functions can be considered, as detailed in [19]. Among them, the so-called *dynamic compliance* [2] has been widely employed. The related TO analyses and derivatives computation can be carried out by neglecting or by considering damping effects, as shown in [20]. It has been observed that the minimisation of the dynamic compliance provides similar results to the classic stiffness maximisation problem, when the driving frequency is lower than the first eigen-frequency. Conversely, special attention should be paid in case of a higher driving frequency or if the dynamic response is evaluated on a range of frequencies (spanning more than one natural frequency of the structure) [6].

Although all the aforementioned complications, solutions to some challenging problems involving dynamics in TO have been proposed in bibliography. A standard ESO formulation is enhanced in [21] by including stress and frequency constraints in order to properly design suspension bridges. An interesting application concerning the optimised design of phononic band-gap materials is provided in [22]. Dynamics-related phenomena have been considered also in the framework of multi-objective formulations: eigen-frequencies and static requirements have been successfully taken into account in [23], whilst the problem of attenuating vibrations by maximising the modal damping ratio is faced in [24]. These concepts have been applied to the design of specific components such as vehicle doors [25]. Eigen-frequencies have been considered in the context of multi-scale problems as well [16]. Other applications involving eigen-frequencies include two-material structures [26], couple-stress continuum [27], geometrically non-linear structures [28]. Cutting-edge problems have been solved also by minimising the harmonic response of a structure: dedicated design strategies of piezoelectric energy harvesting devices [29], the response of structures to wind and seismic loads [30, 31] and the TO optimisation of the interface between acoustic and structural domain [32] have been proposed in the literature.

Beyond the previously discussed numerical issues, a fundamental aspect in TO is the consistency between the optimised configuration and the actual reassembled geometry in a CAD environment. This issue is common to whatever problem formulation in TO (involving static compliance, displacements, eigen-value problems, dynamic responses, etc.) and it needs to be properly overcome in order to achieve a full integration of TO in a design strategy. Several TO methods (SIMP, LSM) make use of FE to carry out the optimisation and the resulting topology is available in the form of an "element-wise" description. Usually, at the end of the optimisation process, a further step is needed for retrieving a smooth iso-contour of the optimised structure. This happens even in the case of LSMs, because the Level-Set Function (the geometric descriptor) is affected by the underlying mesh. This phase is far from being trivial and often implies some approximations, depending on the user's experience. To overcome this difficulty, some authors formulated TO problems in the framework of isogeometric analysis (IGA) [33]. The NURBS curves and surfaces [34] are combined with TO algorithms (SIMP, LSM, ESO) and are used both to describe the geometry being optimised and as a tool to solve the governing equations of the problem at hand [35–38]: accordingly, this constitutes one of the most important advantages of IGA-based TO. On the other hand, the possibility of using the classic FE method to perform TO analyses is still attractive because allows dealing with relatively complex problems, typical of the industrial environment, taking advantage from robust widespread FE software. This is the reason why an approach similar to IGA-based TO (but substantially different) has been recently proposed in [39–42]: the well-established SIMP method and the NURBS theory [34] are combined in order to develop a geometry-based TO algorithm. The main idea behind the SIMP method based on NURBS entities is to embed the whole structure in a suitable design domain and to define the pseudo-density *via* a NURBS entity of dimension $D + 1$, where D is the dimension of the TO problem. This method has proven to be particularly effective when constraints of different technological/geometrical nature are included in the formulation of the optimisation problem [40, 43, 44]. FE are used to evaluate mechanical responses, whilst the NURBS entity of dimension $D + 1$ describes the topology. The intrinsic CAD-compatibility of NURBS entities allows for simplifying the post-processing phase at the end of the optimisation. Since NURBS surfaces can be directly imported in any CAD environment, retrieving the boundary of the optimised structure (and not the pixelised/voxelised one) is a trivial task in 2D and facilities can be provided for the 3D case. Moreover, the NURBS formalism guarantees for a reduction of design variables and there is no need to define artificial filter zones to avoid ill-conditioning phenomena (i.e. the so-called *checker-board effect*), typical of the classical density-based approaches.

The major contribution of this work is the integration of design requirements involving dynamical responses (eigenfrequencies and harmonic analysis) into the NURBS-based SIMP method. Accordingly, it is shown that the method is sound, robust and not limited to the classical problem of compliance minimisation subject to an equality constraint on the volume [40, 41]. All numerical issues related to dynamic problems are efficiently handled by combining classic methodologies with the NURBS formalism. The potential of NURBS entities is fully exploited in terms of CAD-compatibility as well, since the post-processing phase to reassemble the optimised structures in the CAD environment is simplified. Performances of the reassembled structures are compared to those of the corresponding pseudo-density map: results emphasise that the method is globally conservative, in the sense that the configurations reassembled after the post-processing phase have a better objective function than that of the corresponding density maps.

The paper follows this outline. Section 2 gives the fundamentals about the NURBS theory. Section 3 introduces the main concepts and consequences of the NURBS-based SIMP method and it includes the mathematical statement of some dynamics problems in this theoretical framework. Details about the numerical implementation and the advantages of this formalism in the post-processing phase are given in Section 4. The effectiveness of the proposed approach is shown on several 2D and 3D benchmarks in Section 5: a sensitivity analysis of solutions to the NURBS discrete parameters has been carried out too. Finally, Section 6 ends the paper with some meaningful conclusions and prospects.

2. The NURBS hyper-surfaces theory

The fundamentals of NURBS entities are briefly introduced in the most general case of NURBS hyper-surfaces. Curves and surfaces formulae, widely discussed in [34, 45–47], can be easily deduced from the following relations. A NURBS hyper-surface is a polynomial-based function, defined over a *parametric space* (domain), taking values in the *NURBS space* (codomain). Therefore, if N is the dimension of the *parametric space* and M is the dimension of the *NURBS space*, a NURBS entity is defined as $\mathbf{H} : \mathbb{R}^N \longrightarrow \mathbb{R}^M$. For example, one scalar parameter ($N = 1$) can describe both a plane curve ($M = 2$) and a 3D curve ($M = 3$). In the case of a surface, two scalar parameters are needed ($N = 2$) together with, of course, three physical coordinates $M = 3$. The mathematical formula of a generic NURBS hyper-surface is

$$\mathbf{H}(u_1, \ldots, u_N) = \sum_{i_1=0}^{n_1} \cdots \sum_{i_N=0}^{n_N} R_{i_1,\ldots,i_N}(u_1, \ldots, u_N)\mathbf{P}_{i_1,\ldots,i_N}, \tag{1}$$

where $R_{i_1,\ldots,i_N}(u_1, \ldots, u_N)$ are the piecewise rational basis functions, which are related to the standard Bernstein's polynomials $N_{i_k,p_k}(u_k)$, $k = 1, \ldots, N$ by means of the relationship

$$R_{i_1,\ldots,i_N}(u_1, \ldots, u_N) = \frac{w_{i_1,\ldots,i_N} \prod_{k=1}^{N} N_{i_k,p_k}(u_k)}{\sum_{j_1=0}^{n_1} \cdots \sum_{j_N=0}^{n_N} \left[w_{j_1,\ldots,j_N} \prod_{k=1}^{N} N_{j_k,p_k}(u_k) \right]}. \tag{2}$$

In Eqs. (1) and (2) , $\mathbf{H}(u_1, \ldots, u_N)$ is a M-dimension vector-valued rational function, $(u_1, \ldots, u_N)$ are scalar dimensionless parameters defined in the interval $[0, 1]$, whilst $\mathbf{P}_{i_1,\ldots,i_N}$ are the so called *control points*. The j-th control point coordinate ($X^{(j)}_{i_1,\ldots,i_N}$) is stored in the array $\mathbf{X}^{(j)}$, whose dimensions are $(n_1+1)\times\cdots\times(n_N+1)$. The explicit expression of control points coordinates in $\mathbb{R}^M$ is:

$$\begin{gathered}\mathbf{P}_{i_1,\dots,i_N}=\{X^{(1)}_{i_1,\dots,i_N},\dots,X^{(M)}_{i_1,\dots,i_N}\},\\ \mathbf{X}^{(j)}\in\mathbb{R}^{(n_1+1)\times\cdots\times(n_N+1)},\ j=1,\dots,M.\end{gathered}\tag{3}$$

For NURBS surfaces, $\mathbf{P}_{i_1,i_2}=\{X^{(1)}_{i_1,i_2},X^{(2)}_{i_1,i_2},X^{(3)}_{i_1,i_2}\}$ and each coordinate is arranged in a matrix defined in $\mathbb{R}^{(n_1+1)\times(n_2+1)}$. The control points layout is referred as *control polygon* for NURBS curves, *control net* for surfaces and *control hyper-net* otherwise [34]. The generic control point does not actually belong to the NURBS entity but it affects the NURBS shape by means of its coordinates. A suitable scalar quantity $w_{i_1,\dots,i_N}$ (called weight) is related to the respective control point $\mathbf{P}_{i_1,\dots,i_N}$. The higher is the weight $w_{i_1,\dots,i_N}$, the more the NURBS entity is attracted towards the control point $\mathbf{P}_{i_1,\dots,i_N}$. $N_{i_k,p_k}(u_k)$ are also called *blending functions*. For each parametric direction u_k, $k=1,\dots,N$, a specific degree p_k is assigned. The recursive definition of the blending function $N_{i_k,p_k}(u_k)$ is

$$N_{i_k,0}(u_k)=\begin{cases}1 \text{ if } U^{(k)}_{i_k}\le u_k<U^{(k)}_{i_k+1},\\ 0 \text{ otherwise,}\end{cases}\tag{4}$$

$$\begin{gathered}N_{i_k,q}(u_k)=\frac{u_k-U^{(k)}_{i_k}}{U^{(k)}_{i_k+q}-U^{(k)}_{i_k}}N_{i_k,q-1}(u_k)+\frac{U^{(k)}_{i_k+q+1}-u_k}{U^{(k)}_{i_k+q+1}-U^{(k)}_{i_k+1}}N_{i_k+1,q-1}(u_k),\\ q=1,\dots,p_k,\end{gathered}\tag{5}$$

where each constitutive blending function is defined on the knot vector

$$\mathbf{U}^{(k)}=\{\underbrace{0,\dots,0}_{p_k+1},U^{(k)}_{p_k+1},\dots,U^{(k)}_{m_k-p_k-1},\underbrace{1,\dots,1}_{p_k+1}\},\tag{6}$$

whose dimension is m_k+1, with

$$m_k=n_k+p_k+1.\tag{7}$$

Each knot vector $\mathbf{U}^{(k)}$ is a non-decreasing sequence of real numbers that can be interpreted as a discrete collection of values of the related dimensionless parameter u_k. The blending functions are characterised by several interesting properties: the interested reader is addressed to [34] for a deeper insight into the matter. Here, only the *local support property* is recalled because it is of paramount importance for the NURBS-based SIMP method [39–41]:

$$\begin{aligned} &R_{i_1,\ldots,i_N}(u_1,\ldots,u_N) \neq 0 \\ \text{if } (u_1,\ldots,u_N) \in &\left[U^{(1)}_{i_1}, U^{(1)}_{i_1+p_1+1}\right[\times \cdots \times \left[U^{(N)}_{i_N}, U^{(N)}_{i_N+p_N+1}\right[. \end{aligned} \tag{8}$$

Eq. (8) means that each control point (and the respective weight) affects only a precise zone of the *parametric space*, that is precisely referred as *local support* or *influence zone*.

3. The NURBS-based SIMP algorithm for topology optimisation

3.1. Generalities

Standard TO problems involving static analyses have been formulated in the NURBS-based SIMP framework in [39–41]. Here, the most relevant aspects of the method are recalled in order to provide a clear understanding of the formulation of dynamics-related problems in the new context based on NURBS entities. Without loss of generality, the discussion is focused on 3D problems. Let $D \subset \mathbb{R}^3$ be the design domain, i.e. a compact subset in the 3D Euclidean space, in which a Cartesian orthogonal frame $O(x_1, x_2, x_3)$ is defined:

$$D = \{(x_1, x_2, x_3) \in \mathbb{R}^3 : x_1 \in [0, a_1], x_2 \in [0, a_2], x_3 \in [0, a_3]\}, \tag{9}$$

where a_1, a_2 and a_3 are three reference lengths of the domain, defined along x_1, x_2 and x_3 axes, respectively. The pseudo-density determining the optimal material distribution in D is represented by means of a continuous pseudo-density function $\rho(\mathbf{x}) = \rho(x_1, x_2, x_3) \in [0, 1]$ defined on D. Particularly, ρ is evaluated at the centroid $\mathbf{x}_e$ of each element constituting a predefined mesh: $\rho(\mathbf{x}_e) = \rho_e = 1$ means fully dense bulk material, whereas $\rho(\mathbf{x}_e) = \rho_e = 0$ means void phase. The pseudo-density function affects the physical responses of the problem at hand, namely the stiffness tensor E_{ijkl} and the material density γ:

$$E_{ijkl}(\rho(x_1, x_2, x_3)) = f_\omega\left(\rho(x_1, x_2, x_3)\right) E^0_{ijkl}, \quad i, j, k, l = 1, 2, 3, \tag{10}$$

$$\gamma(\rho(x_1, x_2, x_3)) = \rho(x_1, x_2, x_3)\gamma^0. \tag{11}$$

In Eqs. (10)-(11), E^0_{ijkl} and γ^0 are the stiffness tensor and the density, respectively, of the bulk isotropic material. It is noteworthy that the actual density γ is linearly penalised, whilst the stiffness tensor is penalised according to a specific law $f_\omega\left(\rho(x_1, x_2, x_3)\right)$. Often, especially in SIMP methods, f_ω is a simple power law. However, more suited penalisation schemes can be used in dynamics problem to overcome the numerical issue of spurious modes. These aspects are discussed in details in Section 4.

As far as the eigen-frequencies problem is concerned, when the structural damping is neglected, the governing state equation reads:

$$\left(\mathbf{K} - \omega_i^2\mathbf{M}\right)\boldsymbol{\psi}_i = \mathbf{0},\ i = 1, ..., N_m, \tag{12}$$

where $\mathbf{K}$ is the global stiffness matrix of the structure, $\mathbf{M}$ is the global mass matrix, whilst $\boldsymbol{\psi}_i$ is the i-th mode (eigenvector) related to the corresponding eigen-frequency ω_i (N_m is the number of considered modes).

The equation governing the response of a structure undergoing a harmonic load depends, of course, on the time instant. If the transitory behaviour of the structure is neglected and only the steady state response is taken into account, such an equation can be written in a simplified form in the frequency domain as follows

$$\left(\mathbf{K} - \Omega^2\mathbf{M}\right)\mathbf{d} = \mathbf{f}. \tag{13}$$

In Eq. (13), Ω is the driving frequency of the external harmonic load vector $\mathbf{f}$, while $\mathbf{d}$ identifies the steady state response in terms of generalised displacements resulting from the harmonic solicitation.

The global stiffness matrix and the global mass matrix are related to the element stiffness matrix $\mathbf{K}_e$ and to the element mass stiffness matrix $\mathbf{M}_e$, respectively, through

$$\mathbf{K} = \sum_{e=1}^{N_e}\mathbf{K}_e = \sum_{e=1}^{N_e} f_\omega(\rho_e)\mathbf{K}_e^0, \tag{14}$$

$$\mathbf{M} = \sum_{e=1}^{N_e}\mathbf{M}_e + \mathbf{M}_L = \sum_{e=1}^{N_e}\rho_e\mathbf{M}_e^0 + \mathbf{M}_L, \tag{15}$$

which constitute the FE version of Eqs. (10)-(11). In Eq. (14), $\mathbf{K}_e^0$ is the non-penalised element stiffness matrix (accounting for the stiffness tensor of the bulk material) expanded over the whole structure and expressed in the global reference frame of the FE model. Considering Eq. (15), $\mathbf{M}_e^0$ is the non-penalised element mass matrix, whilst $\mathbf{M}_L$ is the matrix related to lumped non-structural masses, i.e. those masses which do not contribute to the global stiffness matrix; of course, also these matrices are expanded over the full set of degrees of freedom (DOFs) of the model and are expressed in the global frame of the analysis.

In the NURBS-based TO method, the pseudo-density field (i.e. the topological descriptor) is represented through a suitable NURBS entity. Therefore, a NURBS surface is used for 2D problems:

$$\rho(u_1, u_2) = \sum_{i_1=0}^{n_1} \sum_{i_2=0}^{n_2} R_{i_1,i_2}(u_1, u_2)\widehat{\rho}_{i_1,i_2}, \tag{16}$$

while a NURBS hyper-surface is necessary for 3D problems:

$$\rho(u_1, u_2, u_3) = \sum_{i_1=0}^{n_1} \sum_{i_2=0}^{n_2} \sum_{i_3=0}^{n_3} R_{i_1,i_2,i_3}(u_1, u_2, u_3)\widehat{\rho}_{i_1,i_2,i_3}. \tag{17}$$

In Eqs. (16) and (17), $R_{i_1,i_2}(u_1, u_2)$ and $R_{i_1,i_2,i_3}(u_1, u_2, u_3)$ are the NURBS rational basis functions, defined according to Eq. (2). Of course, $\rho(u_1, u_2)$ $(N = 2)$ of Eq. (16) represents only the third coordinate of a 3D array $(M = 3)$: the three coordinates in the *NURBS space* are the two spatial coordinates and the pseudo-density. Similarly, $\rho(u_1, u_2, u_3)$ of Eq. (17) constitutes the fourth coordinate of the array $\mathbf{H}(u_1, u_2, u_3)$ in the special case of $N = 3$ and $M = 4$. Moreover, the dimensionless parameters u_1, u_2, and u_3 are directly related to the physical coordinates as follows:

$$u_j = \frac{x_j}{a_j}, j = 1, 2, 3. \tag{18}$$

Control points $\widehat{\rho}_{i_1,i_2}$ are organised in a 2D array (two indices), whilst $\widehat{\rho}_{i_1,i_2,i_3}$ are normally set in a 3D array, according to the NURBS surfaces and hyper-surfaces algorithms [34].

As stated above, there are many parameters affecting the shape of NURBS entities intervening in Eqs. (16) and (17). Among them, the pseudo-density at control points and the related weights are identified as *design variables*. They are arranged in the arrays $\boldsymbol{\xi}_1^{\mathrm{2D}} \in \mathbb{R}^{[(n_1+1)(n_2+1)]\times 1}$ and $\boldsymbol{\xi}_2^{\mathrm{2D}} \in \mathbb{R}^{[(n_1+1)(n_2+1)]\times 1}$ for 2D problems:

$$\begin{aligned} &{\boldsymbol{\xi}_1^{\mathrm{2D}}}^{\mathrm{T}} = \{\widehat{\rho}_{0,0}, \dots, \widehat{\rho}_{n_1,0}, \widehat{\rho}_{0,1}, \dots, \widehat{\rho}_{n_1,1}, \dots, \widehat{\rho}_{n_1,n_2}\}, \\ &\widehat{\rho}_{i_1,i_2} \in [\widehat{\rho}_{min}, \widehat{\rho}_{max}], \quad \forall i_1 = 0, ..., n_1, \quad \forall i_2 = 0, ..., n_2, \end{aligned} \tag{19}$$

$$\begin{aligned} &{\boldsymbol{\xi}_2^{\mathrm{2D}}}^{\mathrm{T}} = \{w_{0,0}, \dots, w_{n_1,0}, w_{0,1}, \dots, w_{n_1,1}, \dots, w_{n_1,n_2}\}, \\ &w_{i_1,i_2} \in [w_{min}, w_{max}], \quad \forall i_1 = 0, ..., n_1, \quad \forall i_2 = 0, ..., n_2. \end{aligned} \tag{20}$$

Analogously, the pseudo-density at control points and weights are collected in the arrays $\boldsymbol{\xi}_1^{\mathrm{3D}} \in \mathbb{R}^{[(n_1+1)(n_2+1)(n_3+1)]\times 1}$ and $\boldsymbol{\xi}_2^{\mathrm{3D}} \in \mathbb{R}^{[(n_1+1)(n_2+1)(n_3+1)]\times 1}$ for 3D applications:

$$\begin{aligned} &{\boldsymbol{\xi}_1^{\mathrm{3D}}}^{\mathrm{T}} = \{\widehat{\rho}_{0,0,0}, \dots, \widehat{\rho}_{n_1,0,0}, \widehat{\rho}_{0,1,0}, \widehat{\rho}_{n_1,1,0}, \dots, \widehat{\rho}_{n_1,n_2,0}, \dots, \widehat{\rho}_{0,0,n_3}, \dots, \widehat{\rho}_{n_1,n_2,n_3}\}, \\ &\widehat{\rho}_{i_1,i_2,i_3} \in [\widehat{\rho}_{min}, \widehat{\rho}_{max}], \quad \forall i_1 = 0, ..., n_1, \quad \forall i_2 = 0, ..., n_2, \quad \forall i_3 = 0, ..., n_3, \end{aligned} \tag{21}$$

$$\begin{aligned} &{\boldsymbol{\xi}_2^{\mathrm{3D}}}^{\mathrm{T}} = \{w_{0,0,0}, \dots, w_{n_1,0,0}, w_{0,1,0}, w_{n_1,1,0}, \dots, w_{n_1,n_2,0}, \dots, w_{0,0,n_3}, \dots, w_{n_1,n_2,n_3}\}, \\ &w_{i_1,i_2,i_3} \in [w_{min}, w_{max}], \quad \forall i_1 = 0, ..., n_1, \quad \forall i_2 = 0, ..., n_2, \quad \forall i_3 = 0, ..., n_3. \end{aligned} \tag{22}$$

For the sake of synthesis, it is useful to define the following array:

$$\boldsymbol{\Xi}^{(l)} = \begin{cases} \boldsymbol{\xi}_l^{2D} \text{ if } N = 2, \\ \boldsymbol{\xi}_l^{3D} \text{ if } N = 3, \end{cases} \quad l = 1, 2. \tag{23}$$

The other NURBS parameters are set at the beginning of the TO analysis and are not optimised. Here below, a concise discussion on the expected effect of these parameters on the final optimum topology is given (more details can be found in [40, 41]).

- *The degrees*: the greater the degree the grater the local support.
- *The control points number*: the greater the number of control points the smaller the local support. On the one hand, this implies smaller topological features, thus better performances can be achieved. On the

other hand, the number of design variables increases and, consequently, an increased computational burden is expected. Of course, the total number of control points is $n_{tot} = (n_1 + 1)(n_2 + 1)$ in 2D and $n_{tot} = (n_1 + 1)(n_2 + 1)(n_3 + 1)$ in 3D.

- *The knot vector*: the non-trivial knot vectors components appearing in Eq. (6) have been uniformly distributed on the interval $[0, 1]$ for both 2D and 3D problems.

- *Spatial coordinates of control points*: The idea is to distribute control points in the Euclidean space in such a way that the NURBS evaluation along the x_j coordinate coincides exactly with x_j, $j = 1, 2, 3$. When B-Spline entities are employed, this requirement can be met thanks to the so-called *Greville's abscissae* for control points spatial coordinates, i.e.
$$\begin{cases} X^{(1)}_{I_1,*,*} = \frac{a_1}{p_1} \sum_{k=0}^{p_1-1} U^{(1)}_{I_1+k+1}, \ I_1 = 0, ..., n_1, \\ X^{(2)}_{*,I_2,*} = \frac{a_2}{p_2} \sum_{k=0}^{p_2-1} U^{(2)}_{I_2+k+1}, \ I_2 = 0, ..., n_2, \\ X^{(3)}_{*,*,I_3} = \frac{a_3}{p_3} \sum_{k=0}^{p_3-1} U^{(3)}_{I_3+k+1}, \ I_3 = 0, ..., n_3. \end{cases} \tag{24}$$
wherein the symbol $*$, replacing two of the three indices, means that the considered Greville's abscissa depends only upon the corresponding knot vector. Eq. (24) holds for 3D problems, whilst only the first two equations must be considered.

3.2. Formulation of the Dynamics Problems-related Requirements

In this subsection, four dynamics problems are stated in the NURBS-based SIMP framework. Their general formulation is

$$\min_{\boldsymbol{\Xi}^{(1)},\boldsymbol{\Xi}^{(2)}} \ F_l(\boldsymbol{\Xi}^{(1)}, \boldsymbol{\Xi}^{(2)}), \ l = 1, 2, 3, 4,$$

subject to:

$$\begin{cases} \text{state equation,} \\ \dfrac{V(\boldsymbol{\Xi}^{(1)}, \boldsymbol{\Xi}^{(2)})}{V_{ref}} = \dfrac{\sum_{e=1}^{N_e} \rho_e V_e}{V_{ref}} = v, \\ \Xi^{(1)}_k \in [\widehat{\rho}_{min}, \widehat{\rho}_{max}], \ \Xi^{(2)}_k \in [w_{min}, w_{max}], \\ \forall k = 1, ..., n_{tot}. \end{cases} \tag{25}$$

In Eq. (25), $F_l(\mathbf{\Xi}^{(1)}, \mathbf{\Xi}^{(2)}),\ l = 1, 2, 3, 4$, is a general objective function that needs to be specified according to the problem at hand.

The problem of maximising the first eigen-frequency subject to an equality constraint on the volume of the structure can be stated by setting

$$F_1(\mathbf{\Xi}^{(1)}, \mathbf{\Xi}^{(2)}) = -\frac{\omega_1(\mathbf{\Xi}^{(1)}, \mathbf{\Xi}^{(2)})}{\omega_{ref}}, \tag{26}$$

in problem (25) and by using Eq. (12) with $N_m = 1$ as a state equation. In Eq. (26), ω_{ref} is the reference eigen-frequency evaluated through the initial guess of design variables.

For some specific applications, the main requirement is the maximisation of the gap between the first and the second eigen-frequencies, to enlarge the frequency range wherein vibration cannot be induced in the structure. Accordingly, the objective function of problem (25) becomes

$$F_2(\mathbf{\Xi}^{(1)}, \mathbf{\Xi}^{(2)}) = -\left(\frac{\omega_2(\mathbf{\Xi}^{(1)}, \mathbf{\Xi}^{(2)}) - \omega_1(\mathbf{\Xi}^{(1)}, \mathbf{\Xi}^{(2)})}{\Delta\omega_{ref}}\right)^2. \tag{27}$$

The state equation is still Eq. (12) with $N_m = 2$. The quantity $\Delta\omega_{ref}$ appearing in Eq. (27) is the difference between the two first eigen-frequencies at iteration 0, and it is used to obtain a dimensionless objective function.

Instead of maximising solely the first eigen-frequency, it could be interesting to maximise the mean value of the first N_f frequencies of a structure:

$$F_3(\mathbf{\Xi}^{(1)}, \mathbf{\Xi}^{(2)}) = -\frac{1}{\overline{\omega}_{ref}} \frac{\sum_{i=1}^{N_f} \omega_i(\mathbf{\Xi}^{(1)}, \mathbf{\Xi}^{(2)})}{N_f}. \tag{28}$$

The main advantage of the formulation of Eq. (28) is that convergence is not as sensitive as in the case of Eq. (26) to the modes switch phenomenon. In Eq. (28), $\overline{\omega}_{ref}$ is a reference mean frequency, evaluated at iteration 0.

A different kind of problem addressed in TO is related to the harmonic response. In this article, the so-called dynamic compliance c_{dyn} is considered as a global response of the structure to the harmonic external load. It can be interpreted as the virtual work of the harmonic external load on the steady state array of DOFs. The objective function of problem (25) reads

$$F_4(\mathbf{\Xi}^{(1)}, \mathbf{\Xi}^{(2)}) = \left(\frac{c_{dyn}(\mathbf{\Xi}^{(1)}, \mathbf{\Xi}^{(2)})}{c_{dyn-ref}}\right)^2 = \left(\frac{\mathbf{f}^T \mathbf{d}(\mathbf{\Xi}^{(1)}, \mathbf{\Xi}^{(2)})}{c_{dyn-ref}}\right)^2, \tag{29}$$

whilst the state equation is given by Eq. (13). In Eq. (29), $c_{dyn-ref}$ is a reference dynamic compliance.

The optimisation of Eq. (25) is subject to an equality constraint on the volume. V represents the volume of the structure, V_e is the volume of element e and V_{ref} is a reference volume. The generic element pseudo-density ρ_e is the pseudo-density evaluated *via* Eqs. (16)-(17) at the element centroid. Of course, the penalisation schemes in the form of Eqs. (14) and (15) are still active. It is noteworthy that the new design variables of problem (25) are the pseudo-densities at the NURBS control points and weights, no longer the element densities like in standard density-based formulations. In the problem statement, $\widehat{\rho}_{min}$ and $\widehat{\rho}_{max}$ represent lower and upper bounds for control points, whereas w_{min} and w_{max} are lower and upper bounds for weights. The initial guess is defined such that, at the first iteration, $\rho_e = v,\ \forall e = 1, ..., N_e$, (where v is the imposed volume fraction): this fact assures that the equality constraint on the volume is met (feasible starting point).

A deterministic algorithm is used to perform the solution search for problem (25). Therefore, the computation of the derivatives of both objective and constraint functions with respect to the design variables in closed form is needed. This task is achieved by exploiting the NURBS *local support property* and the simple chain rule for derivatives calculation. In particular, the local support related to control point $\widehat{\rho}_{I_1,I_2}$ in 2D or $\widehat{\rho}_{I_1,I_2,I_3}$ in 3D can be defined as

$$S_\tau = \begin{cases} S_{I_1,I_2} = \left[U^{(1)}_{I_1}, U^{(1)}_{I_1+p_1+1}\right[\times \left[U^{(2)}_{I_2}, U^{(2)}_{I_2+p_2+1}\right[, \text{ if } N = 2, \\ S_{I_1,I_2,I_3} = \left[U^{(1)}_{I_1}, U^{(1)}_{I_1+p_1+1}\right[\times \left[U^{(2)}_{I_2}, U^{(2)}_{I_2+p_2+1}\right[\times \left[U^{(3)}_{I_3}, U^{(3)}_{I_3+p_3+1}\right[, \text{ if } N = 3. \end{cases} \tag{30}$$

In Eq. (30), the triplet of capital indices (I_1, I_2, I_3) identifies a specific control point or weight with linear index τ given by

$$\tau = \begin{cases} I_1 + I_2(n_1 + 1), \text{ if } N = 2, \\ I_1 + I_2(n_1 + 1) + I_3(n_1 + 1)(n_2 + 1), \text{ if } N = 3. \end{cases} \tag{31}$$

Let Q be a generic scalar function to be considered in a TO problem whose gradient with respect to the generic element pseudo-density, i.e. $\frac{\partial Q}{\partial \rho_e}$, is known. In particular, the derivatives $\frac{\partial F_l}{\partial \rho_e}$ can be easily carried out by means of $\frac{\partial \omega_i}{\partial \rho_e}$ and $\frac{\partial c_{dyn}}{\partial \rho_e}$, which are available in the literature (see, for instance [12, 48]) and reported in Appendix A for the sake of completeness.

In the framework of the NURBS-based SIMP approach, it is required to determine the explicit expressions of $\frac{\partial Q}{\partial \Xi_{\tau}^{(1)}}$ and $\frac{\partial Q}{\partial \Xi_{\tau}^{(2)}}$ that read

$$\frac{\partial Q}{\partial \Xi_{\tau}^{(l)}} = \sum_{e \in S_{\tau}} \frac{\partial Q}{\partial \rho_e} \frac{\partial \rho_e}{\partial \Xi_{\tau}^{(l)}}, \; l = 1, 2. \tag{32}$$

In Eq. (32), only those elements falling into the local support of control point $\Xi_{\tau}^{(1)}$ give a non-null contribution to the derivatives. It can be proven [40, 41] that the derivatives of the NURBS entity with respect to an assigned control point and the related weight take the form

$$\frac{\partial \rho_e}{\partial \Xi_{\tau}^{(1)}} = R_{\tau}^{e}, \tag{33}$$

and

$$\frac{\partial \rho_e}{\partial \Xi_{\tau}^{(2)}} = \frac{R_{\tau}^{e}}{\Xi_{\tau}^{(2)}} \left(\Xi_{\tau}^{(1)} - \rho_e\right). \tag{34}$$

The scalar quantity R_{τ}^{e} appearing in Eqs. (33)-(34) is simply the NURBS rational basis function of Eq. (2), related to control point $\Xi_{\tau}^{(1)}$, evaluated at the element centroid. If Q is replaced by the function at hand, the final expressions of derivatives related to the problems proposed in this paper can be obtained. Therefore, the result of the sensitivity analysis applied to F_1 is given by

$$\frac{\partial F_1}{\partial \Xi_{\tau}^{(1)}} = -\frac{1}{2\kappa_{tot}^{(1)}} \frac{\omega_1}{\omega_{ref}} \sum_{e \in S_{\tau}} \left(\frac{\partial f_{\omega}}{\partial \rho_e} \frac{1}{f_{\omega}} \epsilon_e^{(1)} - \frac{1}{\rho_e} \kappa_e^{(1)} \right) R_{\tau}^{e}, \tag{35}$$

$$\frac{\partial F_1}{\partial \Xi_{\tau}^{(2)}} = -\frac{1}{2\Xi_{\tau}^{(2)} \kappa_{tot}^{(1)}} \frac{\omega_1}{\omega_{ref}} \sum_{e \in S_{\tau}} \left(\frac{\partial f_{\omega}}{\partial \rho_e} \frac{1}{f_{\omega}} \epsilon_e^{(1)} - \frac{1}{\rho_e} \kappa_e^{(1)} \right) \left(\Xi_{\tau}^{(1)} - \rho_e\right) R_{\tau}^{e}. \tag{36}$$

If F_2 is considered, the derivatives read

$$\frac{\partial F_2}{\partial \Xi_{\tau}^{(1)}} = -\frac{2\left(\omega_2 - \omega_1\right)}{\left(\Delta\omega_{ref}\right)^2} \sum_{e \in S_{\tau}} R_{\tau}^{e} \left(\frac{\partial f_{\omega}}{\partial \rho_e} \frac{\delta\omega_{\epsilon-e}^{(1,2)}}{f_{\omega}} - \frac{\delta\omega_{\kappa-e}^{(1,2)}}{\rho_e} \right), \tag{37}$$

$$\frac{\partial F_2}{\partial \Xi_{\tau}^{(2)}} = -\frac{2\left(\omega_2 - \omega_1\right)}{\Xi_{\tau}^{(2)} \left(\Delta\omega_{ref}\right)^2} \sum_{e \in S_{\tau}} R_{\tau}^{e} \left(\Xi_{\tau}^{(1)} - \rho_e\right) \left(\frac{\partial f_{\omega}}{\partial \rho_e} \frac{\delta\omega_{\epsilon-e}^{(1,2)}}{f_{\omega}} - \frac{\delta\omega_{\kappa-e}^{(1,2)}}{\rho_e} \right), \tag{38}$$

where $\delta\omega_{\epsilon-e}^{(i,j)}$ $\delta\omega_{\kappa-e}^{(i,j)}$ are defined as follows:

$$\delta\omega_{\epsilon-e}^{(i,j)} = \frac{1}{2}\left(\frac{\omega_j \epsilon_e^{(j)}}{\kappa_{tot}^{(j)}} - \frac{\omega_i \epsilon_e^{(i)}}{\kappa_{tot}^{(i)}}\right), \tag{39}$$

$$\delta\omega_{\kappa-e}^{(i,j)} = \frac{1}{2}\left(\frac{\omega_j \kappa_e^{(j)}}{\kappa_{tot}^{(j)}} - \frac{\omega_i \kappa_e^{(i)}}{\kappa_{tot}^{(i)}}\right). \tag{40}$$

As far as F_3 is concerned, the expressions of the derivatives are

$$\frac{\partial F_3}{\partial \Xi_\tau^{(1)}} = -\frac{1}{\overline{\omega}_{ref} N_f} \sum_{e \in S_\tau} R_\tau^e \left[\sum_{i=1}^{N_f} \frac{\omega_i}{2\kappa_{tot}^{(i)}} \left(\frac{\partial f_\omega}{\partial \rho_e}\frac{1}{f_\omega}\epsilon_e^{(i)} - \frac{1}{\rho_e}\kappa_e^{(i)}\right)\right], \tag{41}$$

$$\frac{\partial F_3}{\partial \Xi_\tau^{(2)}} = -\frac{1}{\Xi_\tau^{(2)} \overline{\omega}_{ref} N_f} \sum_{e \in S_\tau} R_\tau^e \left(\Xi_\tau^{(1)} - \rho_e\right) \left[\sum_{i=1}^{N_f} \frac{\omega_i}{2\kappa_{tot}^{(i)}} \left(\frac{\partial f_\omega}{\partial \rho_e}\frac{1}{f_\omega}\epsilon_e^{(i)} - \frac{1}{\rho_e}\kappa_e^{(i)}\right)\right]. \tag{42}$$

Finally, the sensitivity analysis of the dynamic compliance related to F_4 gives

$$\frac{\partial F_4}{\partial \Xi_\tau^{(1)}} = -\frac{4c_{dyn}}{c_{dyn-ref}^2} \sum_{e \in S_\tau} R_\tau^e \left(\frac{\partial f_\omega}{\partial \rho_e}\frac{1}{f_\omega}\epsilon_e - \frac{1}{\rho_e}\kappa_e\right), \tag{43}$$

$$\frac{\partial F_4}{\partial \Xi_\tau^{(2)}} = -\frac{4c_{dyn}}{\Xi_\tau^{(2)} c_{dyn-ref}^2} \sum_{e \in S_\tau} R_\tau^e \left(\Xi_\tau^{(1)} - \rho_e\right) \left(\frac{\partial f_\omega}{\partial \rho_e}\frac{1}{f_\omega}\epsilon_e - \frac{1}{\rho_e}\kappa_e\right). \tag{44}$$

In Eqs. (35)-(42), $\kappa_{tot}^{(i)}$ represents the kinetic energy of the whole structure vibrating at ω_i. Under the same conditions, $\kappa_e^{(i)}$ and $\epsilon_e^{(i)}$ are the contributions given by element e to the total kinetic energy and to the total strain energy, respectively. In Eqs. (43)-(44), the upper script disappears because the kinetic energy and the strain energy are related to the structure vibrating at the driving frequency Ω.

The derivatives of the volume with respect to the NURBS control points and weights are trivial and reported here below for the sake of completeness:

$$\frac{\partial}{\partial \Xi_\tau^{(1)}}\left(\frac{V}{V_{ref}}\right) = \frac{1}{V_{ref}} \sum_{e \in S_\tau} V_e R_\tau^e, \tag{45}$$

$$\frac{\partial}{\partial \Xi_{\tau}^{(2)}}\left(\frac{V}{V_{ref}}\right) = \frac{1}{V_{ref}\Xi_{\tau}^{(2)}} \sum_{e \in S_{\tau}} (\Xi_{\tau}^{(1)} - \rho_e) V_e R_{\tau}^{e}. \tag{46}$$

4. Numerical strategy

The NURBS-based TO algorithm is called *SANTO* (SIMP And NURBS for Topology Optimisation). Two versions are available: the kernel routines have been implemented in both MATLAB and PYTHON environments at the I2M laboratory in Bordeaux. The evaluation of mechanical responses is carried out thanks to external FE software. In this work, the ANSYS® Parametric Design Language (APDL) has been used to implement the FE model of the structure. However, the modular structure of the algorithm allows for easily interfacing the core routines with any external FE software. The post-processing phase needs a CAD environment and the CATIA® software has been chosen. A synthetic scheme of the algorithm is provided in the followings. For a deeper insight into the details of SANTO, the reader is addressed to [41].

1. **Problem Setting**. The objective/constraints functions of the problem at hand are set. The regular domain (rectangular in 2D, prismatic in 3D) embedding the structure is chosen.
2. **NURBS Parametrisation**. The TO analysis can be run by using a B-Spline or a NURBS entity.
3. **FE Model Information**. The FE model corresponding to the structure to be optimised is built into a dedicated software and relevant information (elements identifiers, centroids coordinates) is transferred to the main core.
4. **Design domain definition**. Some regions of the design domain can be disregarded during the optimisation: holes (void zones) or functional surfaces (material zones) are usually defined as Non-Design Regions (NDRs). This step guarantees also the possibility to deal with irregular design domains: whatever domain can be embedded in a rectangular or a prismatic compact in 2D and 3D, respectively. Then, zones without matter can be just considered as NDRs [39–41].
5. **Symmetries Application**. Symmetry conditions can be imposed on the NURBS entity even if the mesh of the FE model is not symmetric at all.

6. **Reference Quantities**. Some geometrical/mechanical quantities are defined to get dimensionless values of the objective/constraints functions. This is basic to obtain a consistent stopping criterion for the optimisation algorithm.
7. **Deterministic Optimisation**. The deterministic optimisation is carried out through the "active-set" algorithm [49]. In this paper, the *fmincon* package of Matlab is used [50].
8. **Post-processing**. This phase is necessary in order to retrieve the boundary of the optimised structure at the end of the optimisation process and it is carried out through a threshold operation. The procedure is illustrated in Fig. 1 and summarised in the followings.

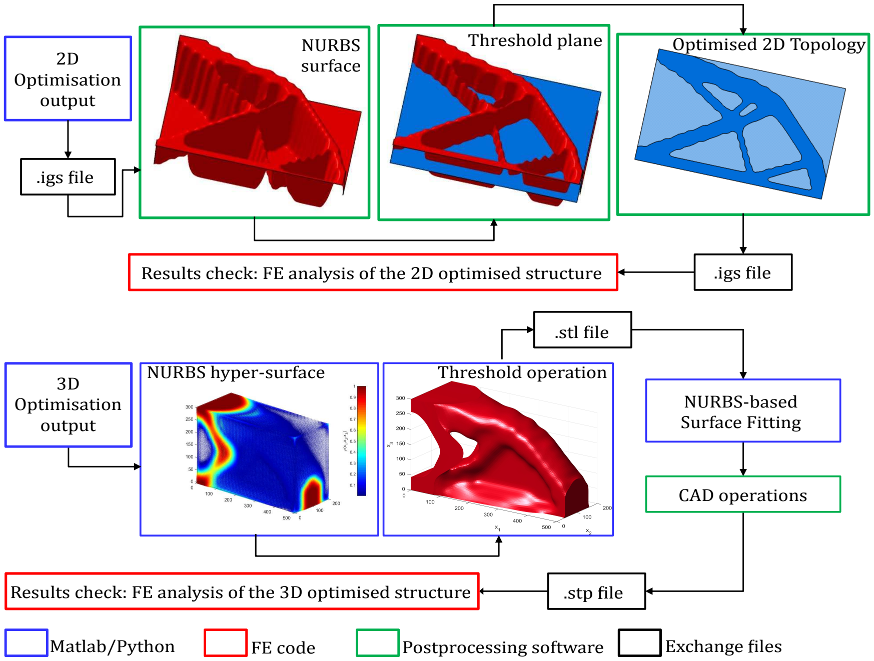

Figure 1: Post-processing phase in SANTO

.

The post-processing is trivial for 2D structures. Firstly, the 3D NURBS surface representing the pseudo-density field is transferred to a CAD software through a standard IGS file. Secondly, a rectangular domain (size $a_1 \times a_2$) is drafted at an altitude corresponding to the threshold value for the density. This threshold value ρ_{th} is chosen in such a

way that the optimisation constraints are met. Finally, the rectangular domain and the NURBS surface are intersected. The final result is fully CAD-compatible and it does not require further geometric operations. Eventually, the consistency of the results can be easily checked by transferring the 2D optimised geometry to the FE solver via a new IGS file.
In 3D, the complexity of the intersection operation increases. The 4D NURBS/B-Spline hyper-surface must be intersected with a suitable hyper-plane corresponding to ρ_{th}. While for 2D structures the intersection takes place in a CAD environment and the results are directly available in terms of geometric entities (the boundary lines), for 3D components such an intersection can be easily performed only in a dedicated environment (e.g. MATLAB/Python) and the result is a *Delaunay triangulation*, which is saved in an STL file. Since the STL file originated from a NURBS hyper-surface, it is characterised by high-quality triangles, without aberrations. This kind of STL files constitutes the basis for a very general and semi-automated surface approximation technique, formulated as an optimisation problem. In this framework, the goal is the minimisation of the distance between a set of sampling points belonging to the 3D topology boundary and those belonging to a set of pertinent NURBS/B-Spline surfaces opportunely connected (in order to correctly describe the boundary). Nevertheless, the most complicated aspect when dealing with such a problem is the determination of a proper *surface parametrisation* for the boundary surfaces of *genus* n [51]. Surface parametrisation for a general surface of *genus* n is a very challenging problem which does not present a unique solution. Inasmuch as good results can be achieved for open surfaces [52], whatever triangulation can be split in several patches (with suitable continuity conditions among them) and a local parametrisation can be provided. Then, the surface fitting is performed through a poly-NURBS entity, where continuity conditions among patches are automatically set. This procedure is detailed in [53].

Some details about the aforementioned points are here discussed for the solution of dynamics problems. Unlike classic SIMP approaches, where the accuracy of the topology description is characterised by the size of the elements of the mesh, the NURBS discrete and continuous parameters are predominant in this method and they have the highest impact on the design [44]. As far as symmetry conditions are concerned, it is remarked that imposing a symmetry on the NURBS is deeply different from imposing symmetries on the FE model. As a matter of fact, imposing a symmetry in the FE framework means, in practice, modelling just one half of the structure and setting suitable boundary conditions (BCs) on the nodes located on the symmetry plane. This implies, on the one hand, that computational time is saved because of the cheaper FE model and, on the other hand, that some information could be lost. In the specific case of eigen-frequencies in TO, if symmetries conditions are set, only symmetric modes are extracted and, consequently, the analysis can be invalidated. Contrariwise, if the whole FE model is considered and symmetry conditions are set on the NURBS representing the pseudo-density, the result will be a symmetric topology undergoing both symmetric and non-symmetric vibrating modes. Furthermore, the symmetry of the NURBS allows for saving computational time because it halves the number of design variables. A synthetic flow-chart of SANTO is provided in Fig. 2.

The first step consists of the NURBS evaluation at the centroids of the elements. Then, the interface between the core of the algorithm and the FE model is handled through some dedicated exchange files, in order to correctly evaluate mechanical quantities and their derivatives with respect to the elements of the mesh. In the case of dynamics-related problems, these derivatives can be written in a very effective way, as shown in Appendix A. This fact implies a very simple structure for the data-exchange files, which do not stock huge stiffness or mass matrices. In the FE software, the penalisation of the mass matrix and of the stiffness matrix are performed by means of a linear law and the polynomial law $f_\omega(\rho_e)$, respectively. If the standard SIMP power law is chosen, the spurious modes issue discussed in Section 1 is not prevented because the stiffness-to-mass ratio goes to zero as $\rho_e^{\alpha-1}$. Inasmuch usually $\alpha = 3$, the local stiffness goes to zero faster than the local mass and, consequently, the result is a spurious, low-frequency mode involving low density regions of the design domain. Without considering an adequate numerical strategy to prevent this phenomenon, the spurious mode is identified as the first eigen-mode and this fact flaws the TO analysis.

In order to overcome this issue, the stiffness matrix is penalised according to the formula suggested in [16]:

$$f_\omega(\rho_e) = 1.1\rho_e^3 - 0.2\rho_e^2 + 0.1\rho_e. \tag{47}$$

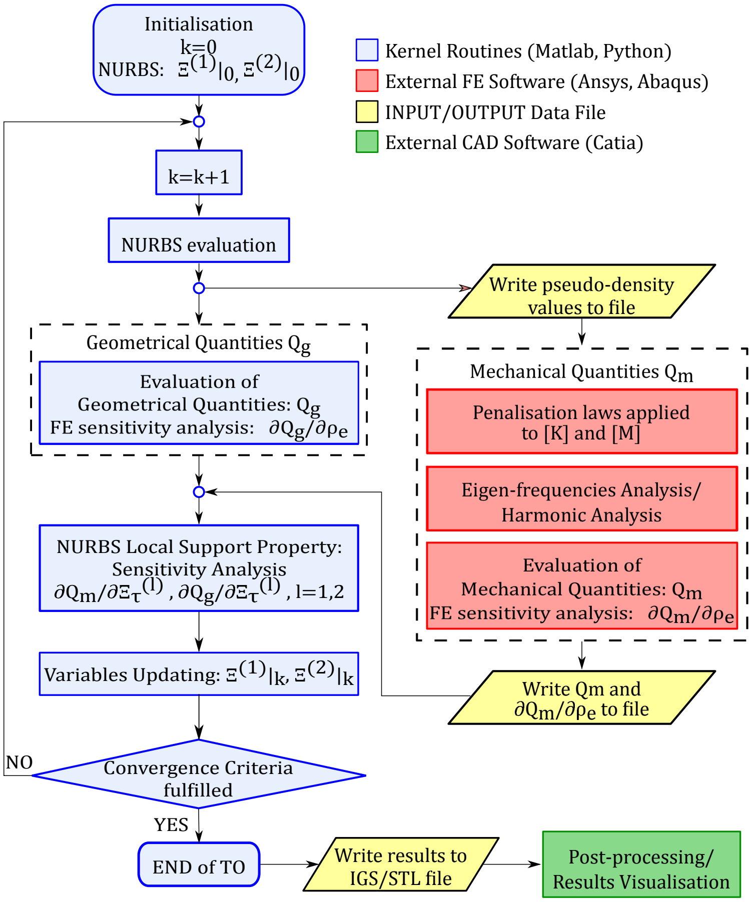

Figure 2: Flow-chart of SANTO for dynamics problems.

As it can be observed from Fig. 3, the ratio f_ω/ρ_e goes to a finite quantity when ρ_e goes to zero. This fact prevents the occurrence of spurious modes and it allows the topology to correctly evolve during the iterations.

As highlighted in Fig. 2, the sensitivity analysis exploits the NURBS local support property to evaluate the analytical form of the gradient, regardless of the nature of the variables at hand. Such a property defines an implicit filter zone, whose size depends on the size of the local support of the blending functions, i.e. on the components of the knot vectors, on the number of control points as well as on the degrees of the basis functions. TO filters create an artificial mutual dependency among the elements densities, i.e. the design variables in the standard SIMP formulation. Conversely, in the case of

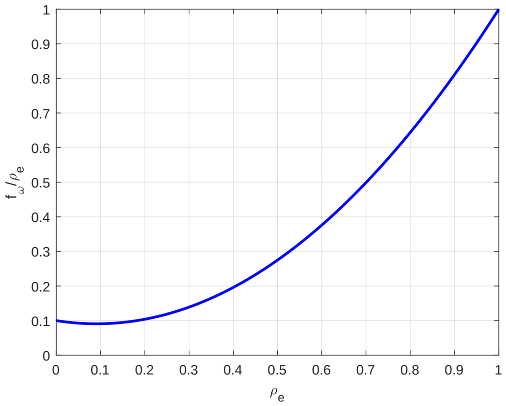

Figure 3: The f_ω/ρ_e ratio.

NURBS, the inter-dependence is automatically provided due to the NURBS local support, without the need of defining a filter on the mesh elements densities [40, 41]. Finally, the convergence is achieved when constraints are met (or barely met, i.e. the optimum solution is on the boundary of the search domain) *and* one of the following conditions occurs: (a) the predicted change of the objective function is lower than a prescribed tolerance (10^{-6}); (b) the norm of the gradient of the Lagrangian functional related to the problem at hand is very close to zero; (c) the predicted change of design variables is lower than a prescribed threshold value (10^{-6}); (d) a maximum value of iterations (set by the user) has been attained. The upper boundary on the iterations number is 400 for the benchmarks discussed in the next section. All these parameters are set in the options of the *fmincon* function.

5. Results

Results provided in this section are related to three benchmarks, which are described hereafter. The aim of the proposed numerical campaign is twofold: on the one hand, the effects of the NURBS parameters on the solution of the TO analysis are investigated. On the other hand, the effectiveness of the presented strategy is shown on 2D and on 3D problems.

5.1. *Benchmarks description*

5.1.1. *A simple plane-stress problem (BK1)*

The first benchmark consists of a thin plate, clamped at both lateral sides. The out-of-plane behaviour is disregarded and a plane-stress formulation is used. An exhaustive description of the problem is provided in Fig. 4 and in its caption. When P4 is solved, a harmonic load $\mathbf{P_h}$ is applied as shown in Fig. 4b and the related exciting frequency is Ω.

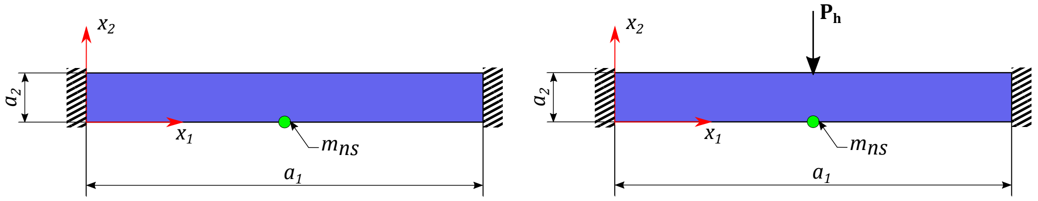

(a) Benchmark BK1 settings in the case of P1, P2 and P3.

(b) Benchmark BK1 settings in the case of P4. $P_h = 100$ N, $\Omega = 100$ Hz.

Figure 4: Benchmark BK1. Geometry: $a_1 = 800$ mm, $a_2 = 100$ mm, Thickness 1 mm. Material: Young Modulus $E = 70000$ MPa, Poisson Modulus $\nu = 0.33$, Density $\gamma = 2.7 * 10^{-9}$ tons/mm^3, Non-structural mass $m_{ns} = 0.001$ tons. Mesh: 160×20 PLANE182 Ansys elements.

5.1.2. *A shell structure (BK2)*

The second benchmark is a 2D square plate accounting for the out-of-plane mechanical behaviour (shell formulation). The plate is clamped along all the four sides, as shown in Fig. 5. Complementary information about the benchmark are collected in the caption of the same figure. The red zones highlighted in Fig. 5 constitute NDRs, i.e. material zones that are neglected during the optimisation. A non-structural mass m_{ns} is associated to the central node of the structure when P1, P2 and P3 are solved. Considering the solution of P4, the non-structural mass is replaced by a harmonic pressure p_h (driving frequency Ω) applied to the green zone shown in Fig. 5b.

5.1.3. *A 3D bridge (BK3)*

A 3D benchmark is proposed in order to emphasise the generality of the procedure outlined in this paper. The test-case is represented in Fig. 6: the upper part of the design domain (in red) is a Non-Design Region and only two small zones are clamped in the bottom part of the design domain.

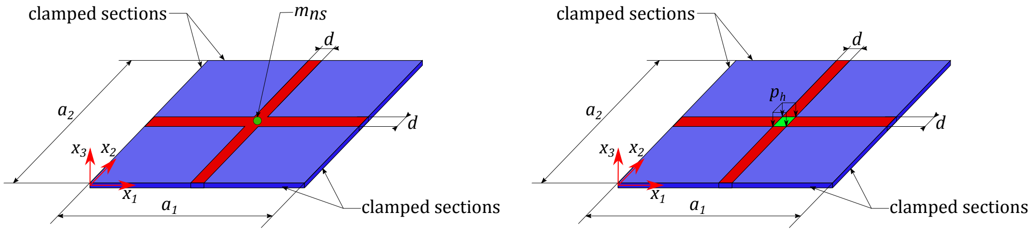

(a) Benchmark BK2 settings in the case of P1, P2 and P3. $m_{ns} = 0.01$ tons.

(b) Benchmark BK2 settings in the case of P4. $p_h = 1$ MPa, $\Omega = 50$ Hz.

Figure 5: Benchmark BK2. Geometry: $a_1 = 320$ mm, $a_2 = 320$ mm, Thickness 2 mm, $d = 20$ mm. Material: Young Modulus $E = 200000$ MPa, Poisson Modulus $\nu = 0.30$, Density $\gamma = 7.8 * 10^{-9}$ tons/mm^3. Mesh: 64×64 SHELL181 Ansys elements.

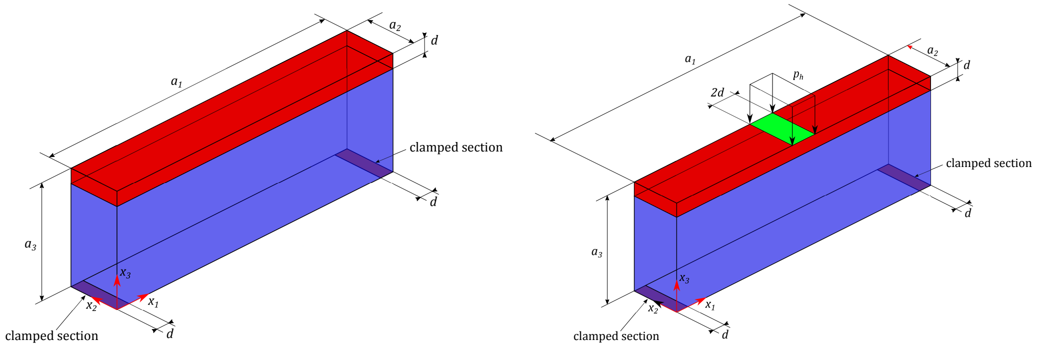

(a) Benchmark BK3 settings in the case of P1, P2 and P3.

(b) Benchmark BK3 settings in the case of P4. $p_h = 1$ MPa, $\Omega = 50$ Hz.

Figure 6: Benchmark BK3. Geometry: $a_1 = 600$ mm, $a_2 = 100$ mm, $a_3 = 200$ mm, $d = 20$ mm. Material: Young Modulus $E = 200000$ MPa, Poisson Modulus $\nu = 0.30$, Density $\gamma = 7.8 * 10^{-9}$ tons/mm^3. Mesh: $90 \times 15 \times 30$ SOLID185 Ansys elements.

Only in the case of P4, a harmonic pressure p_h (driving frequency Ω) is applied on the green zone shown in Fig. 6b.

5.2. Sensitivity of the optimised topology to NURBS discrete parameters for benchmark BK1

The complete set of considered optimisation problems (P1, P2, P3 and P4) is solved several times on benchmark BK1 by choosing different combinations of the NURBS discrete parameters (number of control points and degrees). The goal is to understand the impact of these parameters on the final topologies and to determine which is the real added value of NURBS entities with respect to B-Spline entities. Particularly, the TO is carried out for each combination of the following parameters:

- degrees: $p_k = 2, 3,\ k = 1, 2$;
- number of control points $(n_1 + 1) \times (n_2 + 1) = 64 \times 8,\ 80 \times 10,\ 96 \times 12$;
- weights: inactive (B-Spline), active (NURBS).

The number of design variables depends on the number of control points. Considering the intrinsic symmetry condition of benchmark BK1, the number of design variables is 256, 400, 576 in case of B-Spline entities and 512, 800, 1152 in case of NURBS entities. The number of elements used for the mesh is 3200, and it would correspond to an overall number of 1600 design variables, if a standard SIMP method were used to solve the same problem. Therefore, as remarked in previous studies on the topic [39–41, 44], the NURBS-based SIMP method guarantees for a reduction of design variables. This reduction is at least 28% for benchmark BK1, corresponding to the most detailed design (a NURBS surface with 96×12 control points). If a NURBS surface with 80×10 control points is chosen, the reduction in the number of design variables is 50%.

In the framework of this sensitivity analysis, *density map* solutions and *iso-level* solutions are compared:

- The density-map solution represents the final pseudo-density function, in the form of Eq. (16), which is related to the optimised configuration retrieved at the end of the TO calculation. All the elements of the original mesh are kept and penalised according to the corresponding value of pseudo-density. For each element e, the values of (u_1^e, u_2^e), appearing in Eq. (16), are related to the coordinates of the element centroid, i.e. (x_1^e, x_2^e), through Eq. (18).
- The iso-level solution represents the optimised structure after the post-processing phase: in this case, the objective function is evaluated again on a free mesh built up just on those zones of the design domain related to the solid phase. No penalisation schemes are applied in the case of the iso-level solution.

To facilitate the understanding of the above concepts, the synthetic graphs of Figs. 7, 11, 14 and 18 resume the results: namely, the iso-level solution is represented as a function of the density-map solution. In this particular kind of graph, the plane bisector identifies a critical boundary, which separates two regions of the domain. In the case of problems P1, P2 and P3 (maximisation of a quantity), the upper part of the domain is a conservative region, because the value of the objective function evaluated on the iso-level solution (the actual structure) is higher than that evaluated on the density map solution. Contrariwise, when dealing with the minimisation problem P4, the conservative zone is, of course, the lower part of the domain. In Figs. 7, 11, 14 and 18, the dark grey part of the graph identifies the non-conservative zone.

For each problem, only the most remarkable configurations are reported in this paragraph, whilst the whole set of results is provided in Appendix B to improve the readability of the paper. Finally it must be noticed that, for the sake of brevity, the sensitivity analysis has been carried out only for benchmark BK1.

5.2.1. Solutions of P1

The first eigen-frequency has been evaluated for each optimised topology on the density-map solution and on the iso-level solution. B-Spline solutions are given in Fig. B.1, whilst NURBS solutions are shown in Fig. B.2. The synthesis of numerical results is illustrated in Fig. 7. The reference eigen-frequency is $\omega_{ref} = 2.485$ Hz.

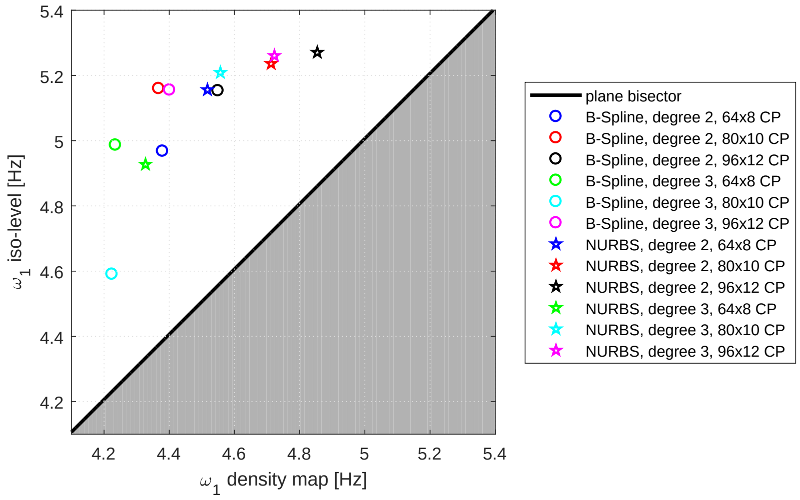

Figure 7: Summary of solutions of P1.

Density-map solutions and iso-level solutions represented in Fig. 7 exhibit some differences in terms of performances. In fact, the points on the graph are not exactly superposed to the plane bisector. This fact is intrinsic to the SIMP method and it is due to the weak phase representing the void in the density map solution. However, it is noteworthy that all the solutions are in the upper part of the domain: therefore, when the threshold operation is performed, the iso-level solution is more efficient than the density-map solution. This is a conservative result.

As far as the sensitivity of the optimised topology to the NURBS discrete parameters is concerned, a NURBS solution offers, in general, better performances than the respective B-Spline solution. This aspect is evident on the graph of Fig. 7 by comparing circle markers and star markers of the same colors. This behaviour is always manifested, except in the case of 64 × 8 control points and degrees 3. This combination of control points and degrees corresponds to the largest size of the local support of the NURBS blending function and, consequently, to the largest size of the filter zone. Under these conditions, solutions exhibit smoother boundaries but convergence is more difficult to achieve. Since one of the stopping criterion of the algorithm is the maximum number of iterations, it can be stated that the NURBS solution characterised by 64 × 8 control points and degree 3 stopped prematurely. It is interesting to remark that the best solution is obtained through a NURBS with 96 × 12 control points and degree 2, which is shown in Fig. 8.

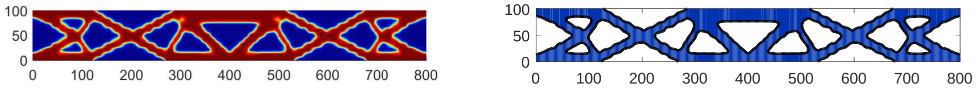

(a) Density map, $\omega_1 = 4.8541$ Hz. (b) Iso-level solution, $\omega_1 = 5.2705$ Hz.

Figure 8: Solution of P1. NURBS, $p_1 = p_2 = 2$, $(n_1 + 1) \times (n_2 + 1) = 96 \times 12$.

When the parametrisation is carried out by means of a B-spline with a too low number of control points, the optimal topology is different and less efficient, as illustrated in Fig. 9.

As a final remark, the solution corresponding to a B-Spline with $(n_1 + 1) \times (n_2 + 1) = 80 \times 10$ and $p_1 = p_2 = 3$ (reported in Fig. 10) shows the worst performances. In particular, a small free-hanging part can be observed in the iso-contour solution of Fig. 10b. This is a clear symptom of a critical size of the filter zone. On the one hand, this size is small enough to promote a more efficient design (with smaller topological details); on the

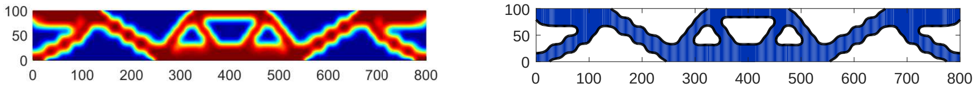

(a) Density map, $\omega_1 = 4.3794$ Hz. (b) Iso-level solution, $\omega_1 = 4.9681$ Hz.

Figure 9: Solution of P1. B-Spline, $p_1 = p_2 = 2$, $(n_1 + 1) \times (n_2 + 1) = 64 \times 8$.

other hand it is still too large to have a fast convergence. Inasmuch as the maximum number of iterations has been set to 400 in this numerical campaign, increasing this limit would surely provide better performances and would probably eliminate the free-hanging part. However, beyond this aspect, both the eigen-frequency and the shape of the vibrating mode have been checked and they are consistent.

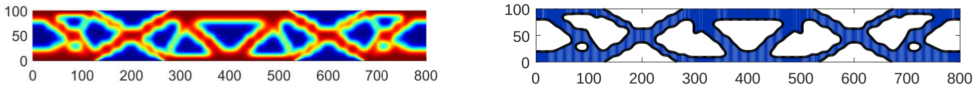

(a) Density map, $\omega_1 = 4.2242$ Hz. (b) Iso-level solution, $\omega_1 = 4.5909$ Hz.

Figure 10: Solution of P1. B-Spline, $p_1 = p_2 = 3$, $(n_1 + 1) \times (n_2 + 1) = 80 \times 10$.

5.2.2. Solutions of P2

The gap between the second and the first eigen-frequencies ($\Delta\omega = \omega_2 - \omega_1$) is computed for optimised topology run on the density-map solution and on the iso-level solution. Results in terms of B-Spline and NURBS solutions are provided Figs. B.3-B.4. Numerical results are summarised in Fig. 11. The value of $\Delta\omega_{ref}$ is 4.265 Hz.

In this case, the points appearing on the graph are less scattered and closer to the plane bisector. Moreover, it can be stated that a NURBS solution is always more efficient than the B-Spline counterpart. Finally, if the best configuration (obtained through a NURBS, $(n_1 + 1) \times (n_2 + 1) = 96 \times 12$, $p_1 = p_2 = 3$) is compared to the worst configuration (B-Spline solution, $(n_1 + 1) \times (n_2 + 1) = 64 \times 8$, $p_1 = p_2 = 3$), there is no evident difference in terms of topologies and the numerical values of $\Delta\omega$ are close as well. The best and the worst solutions are represented in Figs. 12 and 13, respectively.

5.2.3. Solutions of P3

The mean eigen-frequency for benchmark BK1 is just the mean value of the first two eigen-frequencies, i.e. $\overline{\omega} = (\omega_1 + \omega_2)/2$. All results of the

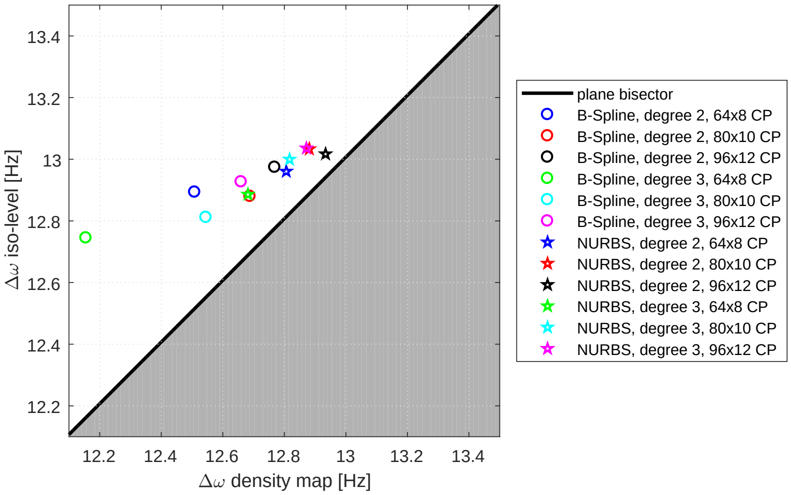

Figure 11: Summary of solutions of P2.

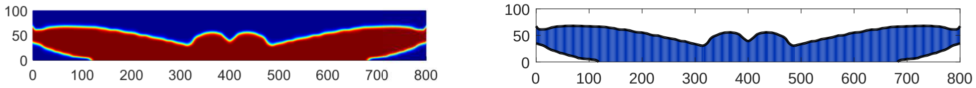

(a) Density map, $\Delta\omega = 12.871744$ Hz.

(b) Iso-level solution, $\Delta\omega = 13.0357$ Hz.

Figure 12: Solution of P2. NURBS, $p_1 = p_2 = 3$, $(n_1 + 1) \times (n_2 + 1) = 96 \times 12$.

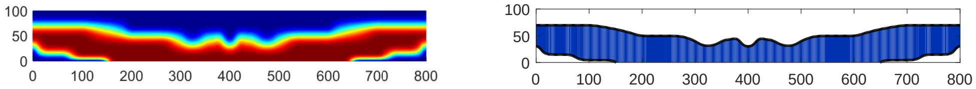

(a) Density map, $\Delta\omega = 12.1551$ Hz.

(b) Iso-level solution, $\Delta\omega = 12.7451$ Hz.

Figure 13: Solution of P2. B-Spline, $p_1 = p_2 = 3$, $(n_1 + 1) \times (n_2 + 1) = 64 \times 8$.

numerical campaign are collected in Fig. 14. The optimised topologies are illustrated in Figs. B.5-B.6. The reference mean frequency is $\overline{\omega_{ref}} = 4.617$ Hz.

When looking at the graph of Fig. 14, it can be observed that many NURBS solutions are clustered around almost the same point. Furthermore, being the optimum topology simple, the higher value of the mean eigen-frequencies is obtained through a rather poor NURBS parametrisation, characterised by just 64×8 control points and degrees 3. In fact, under these conditions, the boundary of the optimised configuration is very smooth

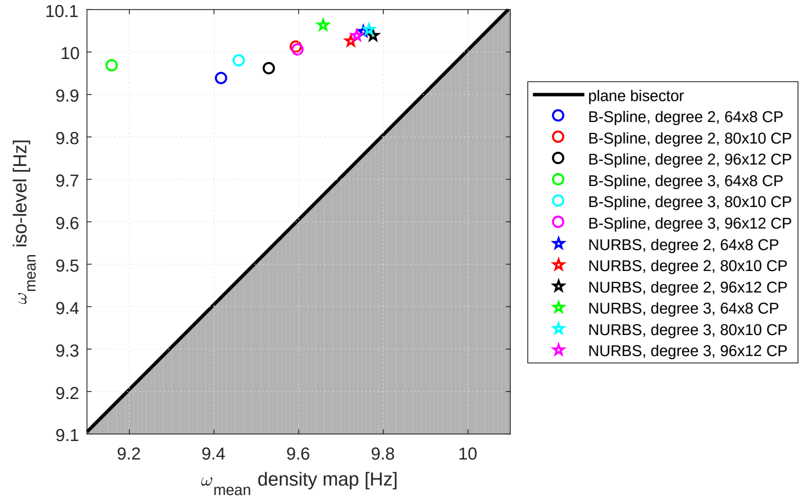

Figure 14: Summary of solutions of P3.

(refer to Fig. 15) and there is no need to exploit a rich (and computationally burdensome) NURBS parametrisation of the computational domain. In contrast, the worst solution, corresponding to a B-Spline parametrisation with $p_1 = p_2 = 2$ and $(n_1 + 1) \times (n_2 + 1) = 64 \times 8$, is reported in Fig. 16.

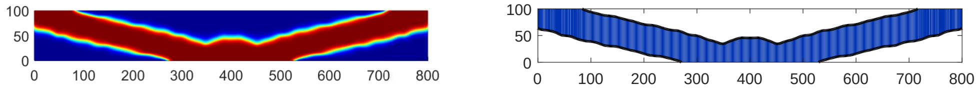

(a) Density map, $\overline{\varpi} = 9.65795$ Hz.

(b) Iso-level solution, $\overline{\varpi} = 10.0633$ Hz.

Figure 15: Solution of P3. NURBS, $p_1 = p_2 = 3$, $(n_1 + 1) \times (n_2 + 1) = 64 \times 8$.

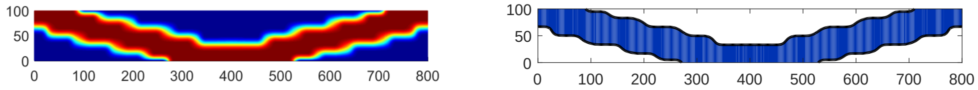

(a) Density map, $\overline{\varpi} = 9.41785$ Hz.

(b) Iso-level solution, $\overline{\varpi} = 9.93755$ Hz.

Figure 16: Solution of P3. B-Spline, $p_1 = p_2 = 2$, $(n_1 + 1) \times (n_2 + 1) = 64 \times 8$.

For the sake of completeness, the trend of the two first eigen-frequencies is represented in Fig. 17 for problems P1, P2 and P3. The graphs are related to the NURBS solution with 96×12 control points and degree 2. Each trend is consistent with the related objective function.

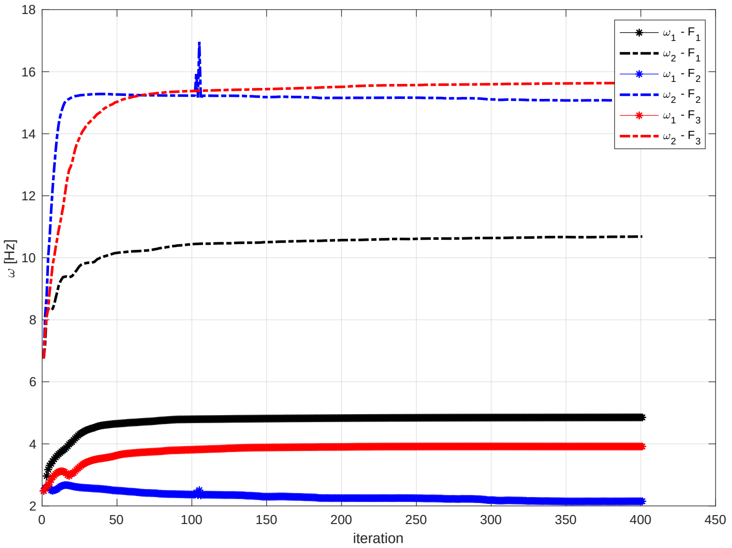

Figure 17: Eigen-frequencies trends - NURBS solution, 96 × 12 control points, degree 2.

5.2.4. Solutions of P4

The dynamic compliance is computed for both the density-map solution and for the iso-level solution. A synthetic overview of results is given in Fig. 18. The related optimised configurations are shown in Figs. B.7-B.8. The reference dynamic compliance is $c_{dyn-ref} = 17.164$ Nmm.

Two aspects deserve a particular attention: firstly, there are several solutions (NURBS and B-Spline) identified by different c_{dyn} of the density map solutions and by an almost identical c_{dyn} of the iso-level solutions. All of them are actually equivalent also in terms of topologies. An example is provided here below in Fig. 19. Secondly, one configuration is not on the conservative part of the domain on the graph of Fig. 18. In fact, the iso-level solution obtained by means of a B-Spline with 64 × 8 control points and degrees 3 is not only the less efficient, but it is also less performing than the respective density-map solution, as highlighted by Fig. 20.

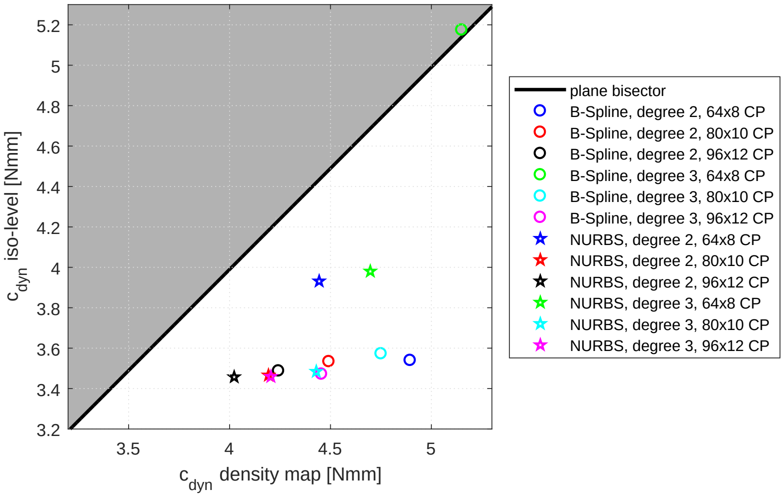

Figure 18: Summary of solutions of P4.

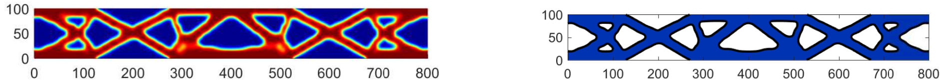

(a) Density map, $c_{dyn} = 4.0228$ Nmm.

(b) Iso-level solution, $c_{dyn} = 3.4572$ Nmm.

Figure 19: Solution of P4. NURBS, $p_1 = p_2 = 2$, $(n_1 + 1) \times (n_2 + 1) = 96 \times 12$.

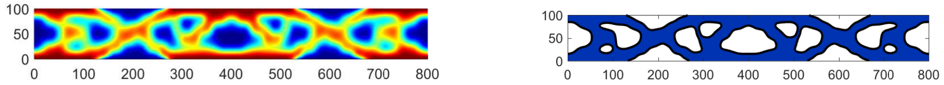

(a) Density map, $c_{dyn} = 5.1502$ Nmm.

(b) Iso-level solution, $c_{dyn} = 5.1743$ Nmm.

Figure 20: Solution of P4. B-Spline, $p_1 = p_2 = 3$, $(n_1 + 1) \times (n_2 + 1) = 64 \times 8$.

5.3. Numerical results for benchmark BK2

In this subsection, the algorithm is applied to benchmark BK2. The solutions of the four problems discussed in this paper are reported in terms of density-map solutions and illustrated in Fig. 21 (NDRs are highlighted in red). All solutions have been obtained by the means of a NURBS surface with $(n_1 + 1) \times (n_2 + 1) = 32 \times 32$ and $p_1 = p_2 = 2$. The physical quantities related to the optimal configurations are given in the captions of the subfigures together with the values of the reference quantities. As far as the problem P3 is concerned, the first four eigen-frequencies are considered to evaluate $\overline{\omega}$.

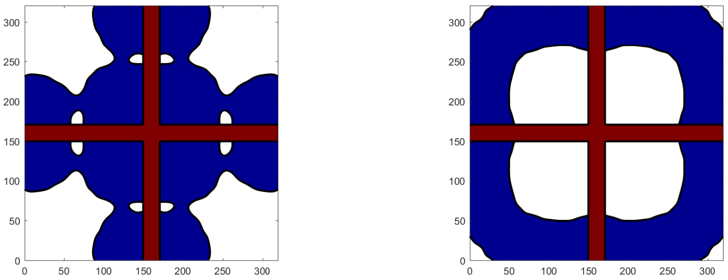

(a) P1, $\omega_{ref} = 14.9493$ Hz, $\omega_1 = 23.1018$ Hz.

(b) P2, $\Delta\omega_{ref} = 220.98$ Hz, $\Delta\omega = 404.60$ Hz.

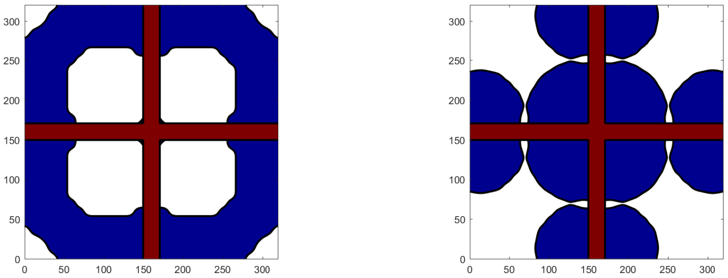

(c) P3, $\overline{\omega_{ref}} = 192.87$ Hz, $\overline{\omega} = 333.03$ Hz.

(d) P4, $c_{dyn-ref} = 2609$ Nmm, $c_{dyn} = 877,75$ Nmm.

Figure 21: Solutions of benchmark BK2 obtained through a NURBS, $(n_1+1)\times(n_2+1) = 32\times 32$, $p_1 = p_2 = 2$.

5.4. Numerical results for benchmark BK3

In this section, results related to benchmark BK3 are shown. The versatility and the effectiveness of the proposed algorithm are proven by solving all the optimisation problems P1, P2, P3 and P4. Numerical and qualitative results are provided Figs. 22-25. All solutions have been carried out by using a B-spline hyper-surface ($(n_1+1)\times(n_2+1)\times(n_3+1) = 60\times10\times20$, $p_1 = p_2 = 2$). Since shapes and topologies of 3D optimised structures are not straightforward to show, two views have been proposed for each problem. In the case of P3, $\overline{\omega} = 1/2(\omega_1+\omega_2)$.

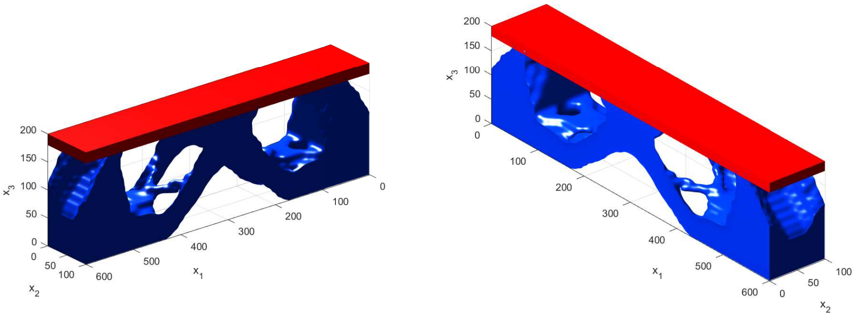

(a) View 1, (b) View 2,

Figure 22: Solutions of P1 on benchmark BK3 obtained through a B-Spline, $(n_1+1)\times(n_2+1)\times(n_3+1) = 60\times10\times20$, $p_1 = p_2 = 2$, $\omega_{ref} = 185.2$ Hz, $\omega_1 = 805.47$ Hz.

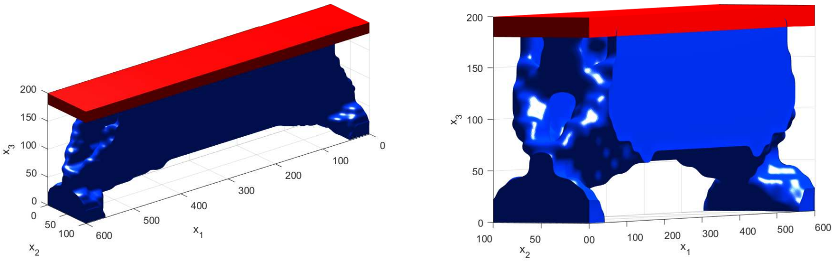

(a) View 1, (b) View 2,

Figure 23: Solutions of P2 on benchmark BK3 obtained through a B-Spline, $(n_1+1)\times(n_2+1)\times(n_3+1) = 60\times10\times20$, $p_1 = p_2 = 2$, $\Delta\omega_{ref} = 269.65$ Hz, $\Delta\omega = 897.382$ Hz.

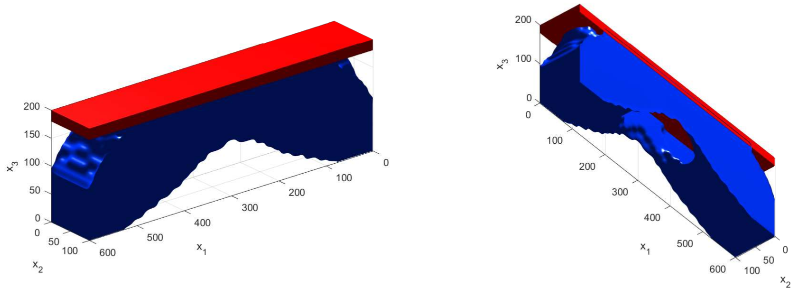

(a) View 1, (b) View 2,

Figure 24: Solutions of P3 on benchmark BK3 obtained through a B-Spline, $(n_1+1)\times(n_2+1)\times(n_3+1) = 60\times 10\times 20$, $p_1 = p_2 = 2$, $\overline{\omega_{ref}} = 632.55$ Hz, $\overline{\omega} = 1017.52$ Hz.

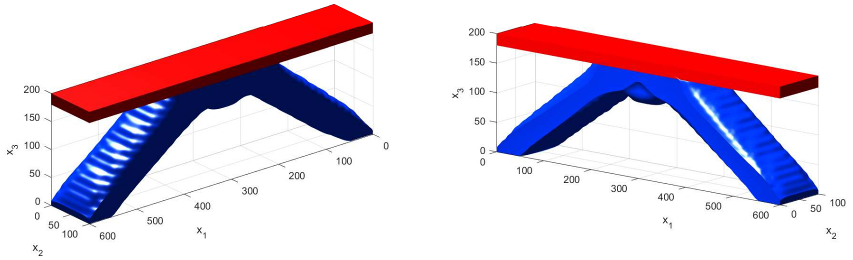

(a) View 1, (b) View 2,

Figure 25: Solutions of P4 on benchmark BK3 obtained through a B-Spline, $(n_1+1)\times(n_2+1)\times(n_3+1) = 60\times 10\times 20$, $p_1 = p_2 = 2$, $c_{dyn-ref} = 63.288$ Nmm, $c_{dyn} = 10.4$ Nmm.

6. Conclusions

This work has shown that TO problems related to structural dynamics can be successfully integrated in an innovative SIMP algorithm based on NURBS entities. In particular, this paper focuses on solving TO problems involving eigen-frequencies and the dynamic compliance. The proposed method exploits both the versatility of NURBS entities and the robustness of the standard finite element method. If compared to IGA, the presented algorithm does not need any *ad hoc* routines to evaluate mechanical responses and it can be easily interfaced with whatever FE software. Meanwhile, the combination of both the NURBS local support property and the classical functional derivatives allows for carrying out the analytical expression of the gradient of the objective function with respect to the new sets of design variables, i.e. the pseudo-density at the control points and the related weights.

The following main points need to be highlighted:

- The new NURBS formalism does not introduce any limitation: eigen-frequencies and dynamic compliance can be easily taken into account to perform TO analyses in 2D and in 3D. Well-known numerical issues characterising eigen-values problems in density-based TO algorithms (spurious modes, mode switching) can be handled by using classical techniques.

- Two main advantages of the NURBS formalism can be clearly identified: when compared to the classical SIMP approach, the number of design variables is reduced, whilst a filter to avoid the checker-board effect is automatically and implicitly provided through the local support of the NURBS blending functions and the CAD reconstruction phase is straightforward.

- A sensitivity analysis of the optimised topology to the NURBS discrete parameters has been performed. Results confirm that an enhanced parametrisation allows for better performances. However, an excellent trade-off between computational cost and effectiveness of the final solution can be achieved by using a number of design variables equal to a half of the number of the mesh elements.

- The comparison of density-map solutions to the iso-level counterparts reveals that the NURBS-based algorithm provides *conservative* and *consistent* solutions. This means that the performances of the actual structure reassembled in the CAD environment are better than those of the related density-map solution and that the equality constraint on the volume is systematically fulfilled on both the density map solution and on the iso-level solution.

As far as prospects are concerned, this paper is far from being exhaustive on the topic of dynamics in TO. As a first step, the NURBS-based approach should be applied to trickier problems, involving transient responses. Moreover, the TO algorithm based on NURBS entities should be extended in order to take into account requirements related to impact dynamics (both high speed and ballistic regimes). An interesting prospect of this study consists of further exploiting the potential of the NURBS formulation in order to avoid some numerical issues related to dynamics. Particularly, the NURBS formalism could allow for precisely tracking the boundary of the optimised structure (like in the LSM). Therefore, the weak phase causing spurious modes would be suppressed and TO would be carried out in an easier way. The crucial condition to take these advantages consists of setting up an effective strategy to update the underlying mesh according to the evolution of the NURBS boundary. Research is ongoing on these aspects.

Acknowledgements

This work benefited from the support of the project COFFA ANR-17-CE10-0008 of the French National Research Agency (ANR).

Data availability

The raw/processed data required to reproduce these findings cannot be shared at this time as the data also forms part of an ongoing study.

Appendix A: Expression of the gradient of dynamic responses

The gradient of the i-th eigen-frequency with respect to the pseudo-density field evaluated at the element centroid, i.e. $\frac{\partial \omega_i}{\partial \rho_e}$, is derived here below. To this purpose, the following relation is inferred from Eq. (12):

$$\boldsymbol{\psi}_i^T \left(\mathbf{K} - \omega_i^2 \mathbf{M}\right) \boldsymbol{\psi}_i = 0. \tag{A.1}$$

Therefore, Eq. (A.1) is derived with respect to the generic element pseudo-density:

$$\begin{aligned} \frac{\partial \boldsymbol{\psi}_i^T}{\partial \rho_e} \left(\mathbf{K} - \omega_i^2 \mathbf{M}\right) \boldsymbol{\psi}_i + \boldsymbol{\psi}_i^T \frac{\partial \left(\mathbf{K} - \omega_i^2 \mathbf{M}\right)}{\partial \rho_e} \boldsymbol{\psi}_i + \\ + \boldsymbol{\psi}_i^T \left(\mathbf{K} - \omega_i^2 \mathbf{M}\right) \frac{\partial \boldsymbol{\psi}_i}{\partial \rho_e} = 0. \end{aligned} \tag{A.2}$$

Taken into account the symmetry of the matrices $\mathbf{K}$ and $\mathbf{M}$ and considering the original Eq. (12), the derivatives $\frac{\partial \boldsymbol{\psi}_i^T}{\partial \rho_e}$ and $\frac{\partial \boldsymbol{\psi}_i}{\partial \rho_e}$ multiply identically null arrays. Consequently Eq. (A.2) simplifies into

$$\boldsymbol{\psi}_i^T \frac{\partial \left(\mathbf{K} - \omega_i^2 \mathbf{M}\right)}{\partial \rho_e} \boldsymbol{\psi}_i = 0, \tag{A.3}$$

that can be expanded as

$$\boldsymbol{\psi}_i^T \frac{\partial \mathbf{K}}{\partial \rho_e} \boldsymbol{\psi}_i - 2\omega_i \frac{\partial \omega_i}{\partial \rho_e} \boldsymbol{\psi}_i^T \mathbf{M} \boldsymbol{\psi}_i - \omega_i^2 \boldsymbol{\psi}_i^T \frac{\partial \mathbf{M}}{\partial \rho_e} \boldsymbol{\psi}_i = 0. \tag{A.4}$$

Moreover, the strain energy and the kinetic energy of the structure vibrating at ω_i can be defined as

$$\epsilon_{tot}^{(i)} = \frac{1}{2} \boldsymbol{\psi}_i^T \mathbf{K} \boldsymbol{\psi}_i = \sum_{e=1}^{N_e} \epsilon_e^{(i)} = \sum_{e=1}^{N_e} \frac{1}{2} \boldsymbol{\psi}_i^T \mathbf{K}_e \boldsymbol{\psi}_i, \tag{A.5}$$

and

$$\kappa_{tot}^{(i)} = \frac{\omega_i^2}{2} \boldsymbol{\psi}_i^T \mathbf{M} \boldsymbol{\psi}_i = \sum_{e=1}^{N_e} \kappa_e^{(i)} = \sum_{e=1}^{N_e} \frac{\omega_i^2}{2} \boldsymbol{\psi}_i^T \mathbf{M}_e \boldsymbol{\psi}_i, \tag{A.6}$$

respectively. In the light of Eqs. (14)-(15), it is straightforward to arrange Eq. (A.4) and to obtain

$$\frac{4\kappa_{tot}^i}{\omega_i} \frac{\partial \omega_i}{\partial \rho_e} = \frac{\partial f_\omega}{\partial \rho_e} \frac{1}{f_\omega} \boldsymbol{\psi}_i^T \mathbf{K}_e \boldsymbol{\psi}_i - \frac{1}{\rho_e} \omega_i^2 \boldsymbol{\psi}_i^T \mathbf{M}_e \boldsymbol{\psi}_i. \tag{A.7}$$

Finally, the gradient of the i-th eigen-frequency can be expressed as

$$\frac{\partial \omega_i}{\partial \rho_e} = \frac{\omega_i}{2\kappa_{tot}^i}\left(\frac{\partial f_\omega}{\partial \rho_e}\frac{1}{f_\omega}\epsilon_e^i - \frac{1}{\rho_e}\kappa_e^i\right), \; e = 1, \ldots, N_e. \tag{A.8}$$

By following a similar procedure, the expression of $\frac{\partial c_{dyn}}{\partial \rho_e}$ can be easily inferred. The first step is

$$\frac{\partial}{\partial \rho_e}\left(\frac{c_{dyn}}{c_{dyn-ref}}\right)^2 = 2\frac{c_{dyn}}{c_{dyn-ref}^2}\frac{\partial c_{dyn}}{\partial \rho_e}. \tag{A.9}$$

The term $\frac{\partial c_{dyn}}{\partial \rho_e}$ appearing in Eq. (A.9) can be evaluated by the definition of c_{dyn}:

$$\frac{\partial c_{dyn}}{\partial \rho_e} = \frac{\partial}{\partial \rho_e}\left(\mathbf{f}^T\mathbf{d}\right) = \mathbf{f}^T\frac{\partial \mathbf{d}}{\partial \rho_e}. \tag{A.10}$$

In Eq. (A.10), it has been assumed that the vector of external harmonic loads does not depend on the element density. By differentiating the state equation (13), one obtains

$$\left(\frac{\partial \mathbf{K}}{\partial \rho_e} - \Omega^2\frac{\partial \mathbf{M}}{\partial \rho_e}\right)\mathbf{d} + \left(\mathbf{K} - \Omega^2\mathbf{M}\right)\frac{\partial \mathbf{d}}{\partial \rho_e} = \mathbf{0}. \tag{A.11}$$

It is straightforward to show, by combining Eq. (A.11) with Eq. (A.10), that

$$\frac{\partial c_{dyn}}{\partial \rho_e} = -\mathbf{d}^T\left(\frac{\partial \mathbf{K}}{\partial \rho_e} - \Omega^2\frac{\partial \mathbf{M}}{\partial \rho_e}\right)\mathbf{d}, \tag{A.12}$$

and, recalling Eqs. (14)-(15), the final expression of the derivative of the square of the dynamic compliance with respect to the element density is

$$\frac{\partial}{\partial \rho_e}\left(\frac{c_{dyn}}{c_{dyn-ref}}\right)^2 = -4\frac{c_{dyn}}{c_{dyn-ref}^2}\left(\frac{\partial f_\omega}{\partial \rho_e}\frac{1}{f_\omega}\epsilon_e - \frac{1}{\rho_e}\kappa_e\right), \; e = 1, ..., N_e. \tag{A.13}$$

Appendix B: Complete set of results on benchmark BK1

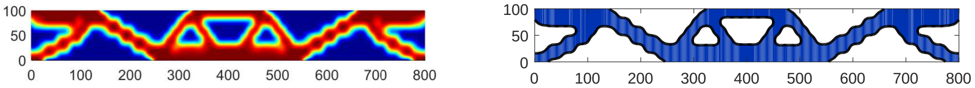

(a) Density map, $p_1 = p_2 = 2$, $(n_1 + 1) \times (n_2 + 1) = 64 \times 8$, $\omega_1 = 4.3794$ Hz.

(b) Iso-level solution, $p_1 = p_2 = 2$, $(n_1 + 1) \times (n_2 + 1) = 64 \times 8$, $\omega_1 = 4.9681$ Hz.

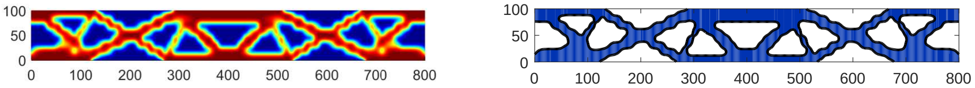

(c) Density map, $p_1 = p_2 = 2$, $(n_1 + 1) \times (n_2 + 1) = 80 \times 10$, $\omega_1 = 4.3675$ Hz.

(d) Iso-level solution, $p_1 = p_2 = 2$, $(n_1 + 1) \times (n_2 + 1) = 80 \times 10$, $\omega_1 = 5.1602$ Hz.

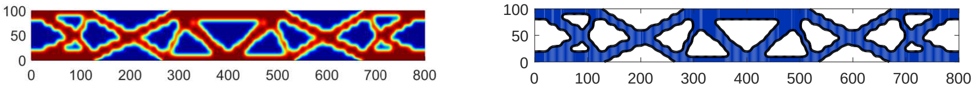

(e) Density map, $p_1 = p_2 = 2$, $(n_1 + 1) \times (n_2 + 1) = 96 \times 12$, $\omega_1 = 4.5494$ Hz.

(f) Iso-level solution, $p_1 = p_2 = 2$, $(n_1 + 1) \times (n_2 + 1) = 96 \times 12$, $\omega_1 = 5.1534$ Hz.

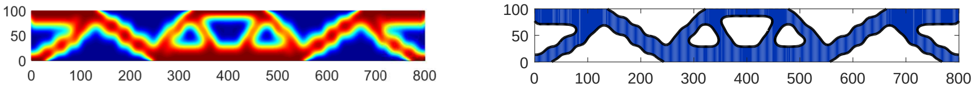

(g) Density map, $p_1 = p_2 = 3$, $(n_1 + 1) \times (n_2 + 1) = 64 \times 8$, $\omega_1 = 4.2349$ Hz.

(h) Iso-level solution, $p_1 = p_2 = 3$, $(n_1 + 1) \times (n_2 + 1) = 64 \times 8$, $\omega_1 = 4.9867$ Hz.

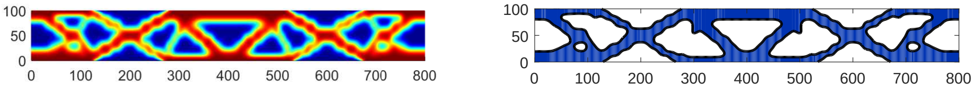

(i) Density map, $p_1 = p_2 = 3$, $(n_1 + 1) \times (n_2 + 1) = 80 \times 10$, $\omega_1 = 4.2242$ Hz.

(j) Iso-level solution, $p_1 = p_2 = 3$, $(n_1 + 1) \times (n_2 + 1) = 80 \times 10$, $\omega_1 = 4.5909$ Hz.

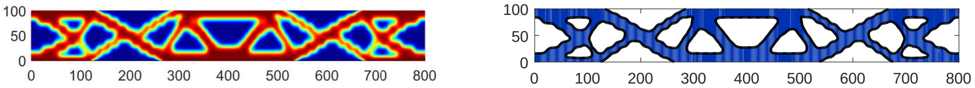

(k) Density map, $p_1 = p_2 = 3$, $(n_1 + 1) \times (n_2 + 1) = 96 \times 12$, $\omega_1 = 4.4009$ Hz.

(l) Iso-level solution, $p_1 = p_2 = 3$, $(n_1 + 1) \times (n_2 + 1) = 96 \times 12$, $\omega_1 = 5.1555$ Hz.

Figure B.1: B-Spline solutions of P1.

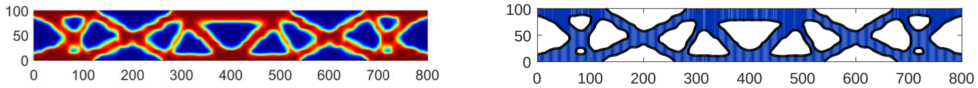

(a) Density map, $p_1 = p_2 = 2$, $(n_1+1)\times(n_2+1) = 64\times 8$, $\omega_1 = 4.5172$ Hz.

(b) Iso-level solution, $p_1 = p_2 = 2$, $(n_1+1)\times(n_2+1) = 64\times 8$, $\omega_1 = 5.1558$ Hz.

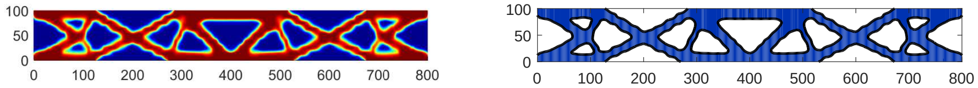

(c) Density map, $p_1 = p_2 = 2$, $(n_1+1)\times(n_2+1) = 80\times 10$, $\omega_1 = 4.7126$ Hz.

(d) Iso-level solution, $p_1 = p_2 = 2$, $(n_1+1)\times(n_2+1) = 80\times 10$, $\omega_1 = 5.2362$ Hz.

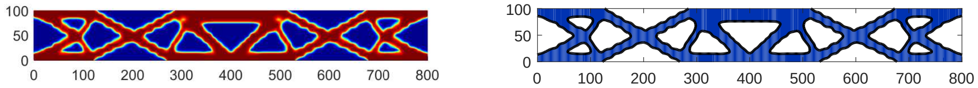

(e) Density map, $p_1 = p_2 = 2$, $(n_1+1)\times(n_2+1) = 96\times 12$, $\omega_1 = 4.8541$ Hz.

(f) Iso-level solution, $p_1 = p_2 = 2$, $(n_1+1)\times(n_2+1) = 96\times 12$, $\omega_1 = 5.2705$ Hz.

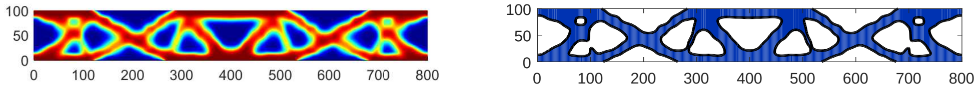

(g) Density map, $p_1 = p_2 = 3$, $(n_1+1)\times(n_2+1) = 64\times 8$, $\omega_1 = 4.3272$ Hz.

(h) Iso-level solution, $p_1 = p_2 = 3$, $(n_1+1)\times(n_2+1) = 64\times 8$, $\omega_1 = 4.9272$ Hz.

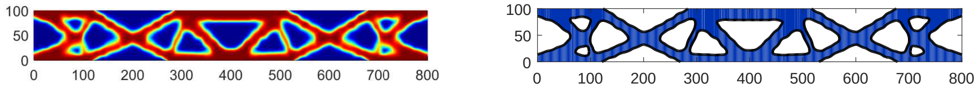

(i) Density map, $p_1 = p_2 = 3$, $(n_1+1)\times(n_2+1) = 80\times 10$, $\omega_1 = 4.5569$ Hz.

(j) Iso-level solution, $p_1 = p_2 = 3$, $(n_1+1)\times(n_2+1) = 80\times 10$, $\omega_1 = 5.2087$ Hz.

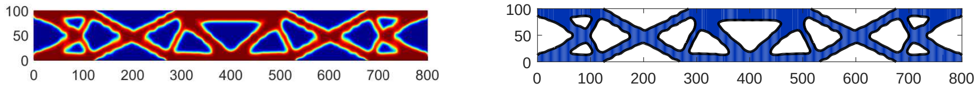

(k) Density map, $p_1 = p_2 = 3$, $(n_1+1)\times(n_2+1) = 96\times 12$, $\omega_1 = 4.7226$ Hz.

(l) Iso-level solution, $p_1 = p_2 = 3$, $(n_1+1)\times(n_2+1) = 96\times 12$, $\omega_1 = 5.2604$ Hz.

Figure B.2: NURBS solutions of P1.

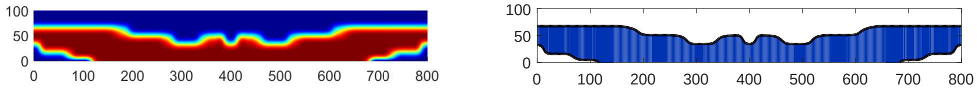

(a) Density map, $p_1 = p_2 = 2$, $(n_1+1) \times (n_2+1) = 64 \times 8$, $\Delta\omega = 12.5085$ Hz.

(b) Iso-level solution, $p_1 = p_2 = 2$, $(n_1+1) \times (n_2+1) = 64 \times 8$, $\Delta\omega = 12.8936$ Hz.

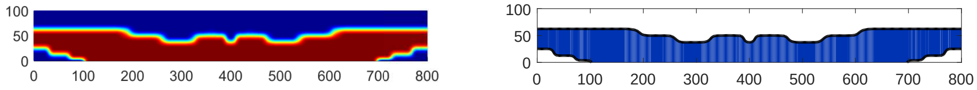

(c) Density map, $p_1 = p_2 = 2$, $(n_1+1) \times (n_2+1) = 80 \times 10$, $\Delta\omega = 12.6882$ Hz.

(d) Iso-level solution, $p_1 = p_2 = 2$, $(n_1+1) \times (n_2+1) = 80 \times 10$, $\Delta\omega = 12.8798$ Hz.

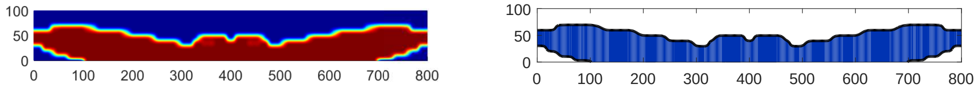

(e) Density map, $p_1 = p_2 = 2$, $(n_1+1) \times (n_2+1) = 96 \times 12$, $\Delta\omega = 12.7687$ Hz.

(f) Iso-level solution, $p_1 = p_2 = 2$, $(n_1+1) \times (n_2+1) = 96 \times 12$, $\Delta\omega = 12.9742$ Hz.

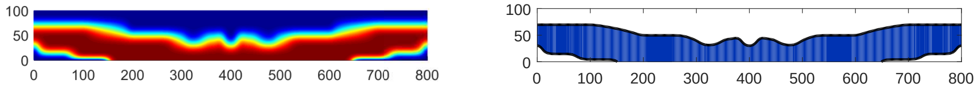

(g) Density map, $p_1 = p_2 = 3$, $(n_1+1) \times (n_2+1) = 64 \times 8$, $\Delta\omega = 12.1551$ Hz.

(h) Iso-level solution, $p_1 = p_2 = 3$, $(n_1+1) \times (n_2+1) = 64 \times 8$, $\Delta\omega = 12.7451$ Hz.

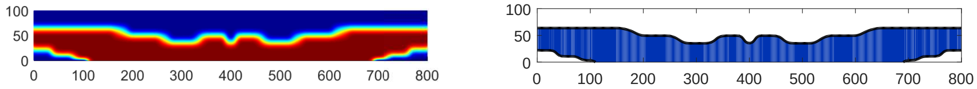

(i) Density map, $p_1 = p_2 = 3$, $(n_1+1) \times (n_2+1) = 80 \times 10$, $\Delta\omega = 12.5452$ Hz.

(j) Iso-level solution, $p_1 = p_2 = 3$, $(n_1+1) \times (n_2+1) = 80 \times 10$, $\Delta\omega = 12.8118$ Hz.

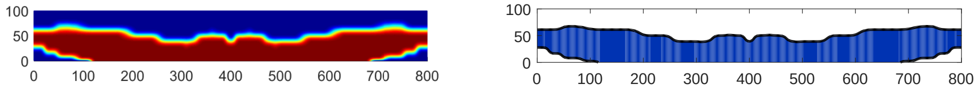

(k) Density map, $p_1 = p_2 = 3$, $(n_1+1) \times (n_2+1) = 96 \times 12$, $\Delta\omega = 12.6596$ Hz.

(l) Iso-level solution, $p_1 = p_2 = 3$, $(n_1+1) \times (n_2+1) = 96 \times 12$, $\Delta\omega = 12.927$ Hz.

Figure B.3: B-Spline solutions of P2.

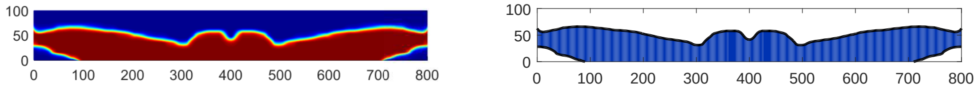

(a) Density map, $p_1 = p_2 = 2$, $(n_1 + 1) \times (n_2 + 1) = 64 \times 8$, $\Delta\omega = 12.80633$ Hz.

(b) Iso-level solution, $p_1 = p_2 = 2$, $(n_1 + 1) \times (n_2 + 1) = 64 \times 8$, $\Delta\omega = 12.9605$ Hz.

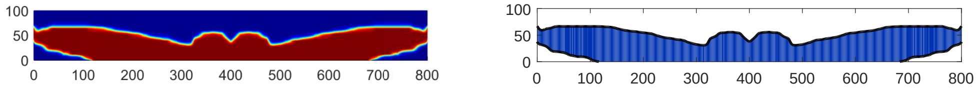

(c) Density map, $p_1 = p_2 = 2$, $(n_1 + 1) \times (n_2 + 1) = 80 \times 10$, $\Delta\omega = 12.8812$ Hz.

(d) Iso-level solution, $p_1 = p_2 = 2$, $(n_1 + 1) \times (n_2 + 1) = 80 \times 10$, $\Delta\omega = 13.0331$ Hz.

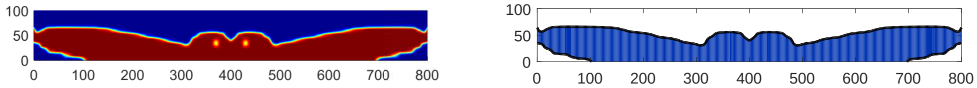

(e) Density map, $p_1 = p_2 = 2$, $(n_1 + 1) \times (n_2 + 1) = 96 \times 12$, $\Delta\omega = 12.934$ Hz.

(f) Iso-level solution, $p_1 = p_2 = 2$, $(n_1 + 1) \times (n_2 + 1) = 96 \times 12$, $\Delta\omega = 13.0168$ Hz.

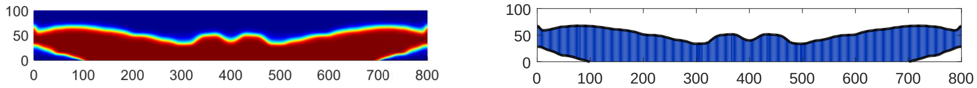

(g) Density map, $p_1 = p_2 = 3$, $(n_1 + 1) \times (n_2 + 1) = 64 \times 8$, $\Delta\omega = 12.6818$ Hz.

(h) Iso-level solution, $p_1 = p_2 = 3$, $(n_1 + 1) \times (n_2 + 1) = 64 \times 8$, $\Delta\omega = 12.8858$ Hz.

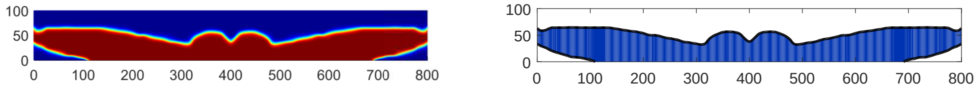

(i) Density map, $p_1 = p_2 = 3$, $(n_1 + 1) \times (n_2 + 1) = 80 \times 10$, $\Delta\omega = 12.817$ Hz.

(j) Iso-level solution, $p_1 = p_2 = 3$, $(n_1 + 1) \times (n_2 + 1) = 80 \times 10$, $\Delta\omega = 12.9993$ Hz.

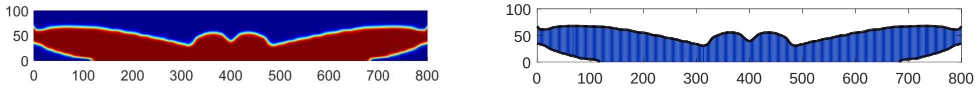

(k) Density map, $p_1 = p_2 = 3$, $(n_1 + 1) \times (n_2 + 1) = 96 \times 12$, $\Delta\omega = 12.871744$ Hz.

(l) Iso-level solution, $p_1 = p_2 = 3$, $(n_1 + 1) \times (n_2 + 1) = 96 \times 12$, $\Delta\omega = 13.0357$ Hz.

Figure B.4: NURBS solutions of P2.

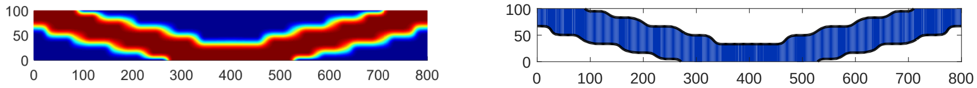

(a) Density map, $p_1 = p_2 = 2$, $(n_1+1)\times(n_2+1) = 64\times 8$, $\overline{\varpi} = 9.41785$ Hz.

(b) Iso-level solution, $p_1 = p_2 = 2$, $(n_1+1)\times(n_2+1) = 64\times 8$, $\overline{\varpi} = 9.93755$ Hz.

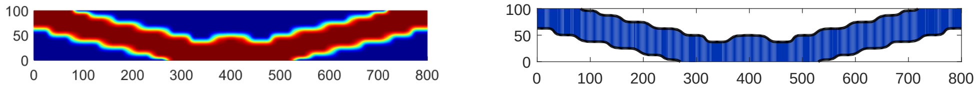

(c) Density map, $p_1 = p_2 = 2$, $(n_1+1)\times(n_2+1) = 80\times 10$, $\overline{\varpi} = 9.5944$ Hz.

(d) Iso-level solution, $p_1 = p_2 = 2$, $(n_1+1)\times(n_2+1) = 80\times 10$, $\overline{\varpi} = 10.01165$ Hz.

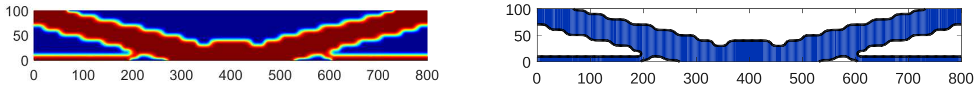

(e) Density map, $p_1 = p_2 = 2$, $(n_1+1)\times(n_2+1) = 96\times 12$, $\overline{\varpi} = 9.53065$ Hz.

(f) Iso-level solution, $p_1 = p_2 = 2$, $(n_1+1)\times(n_2+1) = 96\times 12$, $\overline{\varpi} = 9.96075$ Hz.

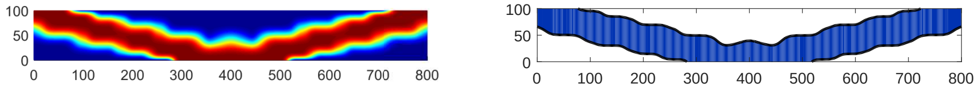

(g) Density map, $p_1 = p_2 = 3$, $(n_1+1)\times(n_2+1) = 64\times 8$, $\overline{\varpi} = 9.15945$ Hz.

(h) Iso-level solution, $p_1 = p_2 = 3$, $(n_1+1)\times(n_2+1) = 64\times 8$, $\overline{\varpi} = 9.96765$ Hz.

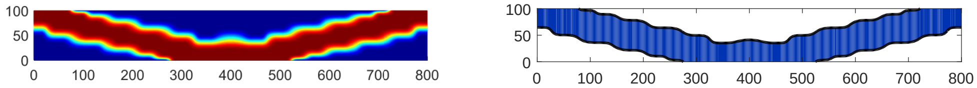

(i) Density map, $p_1 = p_2 = 3$, $(n_1+1)\times(n_2+1) = 80\times 10$, $\overline{\varpi} = 9.45955$ Hz.

(j) Iso-level solution, $p_1 = p_2 = 3$, $(n_1+1)\times(n_2+1) = 80\times 10$, $\overline{\varpi} = 9.9793$ Hz.

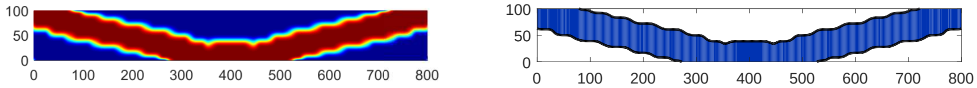

(k) Density map, $p_1 = p_2 = 3$, $(n_1+1)\times(n_2+1) = 96\times 12$, $\overline{\varpi} = 9.5984$ Hz.

(l) Iso-level solution, $p_1 = p_2 = 3$, $(n_1+1)\times(n_2+1) = 96\times 12$, $\overline{\varpi} = 10.005$ Hz.

Figure B.5: B-Spline solutions of P3.

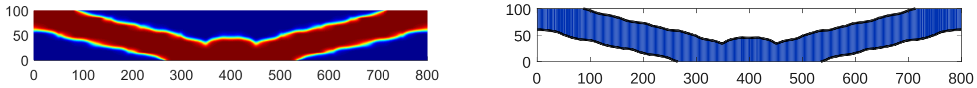

(a) Density map, $p_1 = p_2 = 2$, $(n_1 + 1) \times (n_2 + 1) = 64 \times 8$, $\overline{\varpi} = 9.7527$ Hz.

(b) Iso-level solution, $p_1 = p_2 = 2$, $(n_1 + 1) \times (n_2 + 1) = 64 \times 8$, $\overline{\varpi} = 10.0482$ Hz.

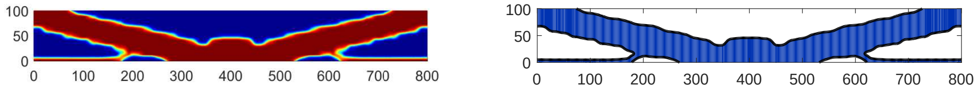

(c) Density map, $p_1 = p_2 = 2$, $(n_1 + 1) \times (n_2 + 1) = 80 \times 10$, $\overline{\varpi} = 9.7233$ Hz.

(d) Iso-level solution, $p_1 = p_2 = 2$, $(n_1 + 1) \times (n_2 + 1) = 80 \times 10$, $\overline{\varpi} = 10.02585$ Hz.

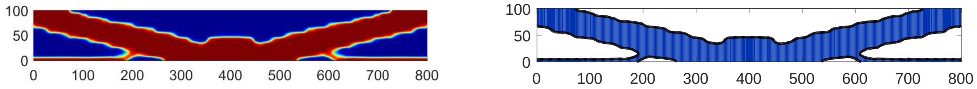

(e) Density map, $p_1 = p_2 = 2$, $(n_1 + 1) \times (n_2 + 1) = 96 \times 12$, $\overline{\varpi} = 9.7758$ Hz.

(f) Iso-level solution, $p_1 = p_2 = 2$, $(n_1 + 1) \times (n_2 + 1) = 96 \times 12$, $\overline{\varpi} = 10.0388$ Hz.

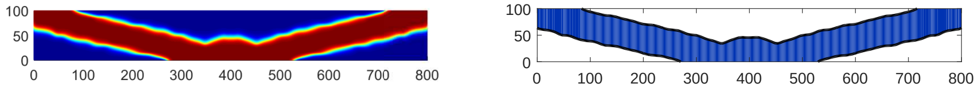

(g) Density map, $p_1 = p_2 = 3$, $(n_1 + 1) \times (n_2 + 1) = 64 \times 8$, $\overline{\varpi} = 9.65795$ Hz.

(h) Iso-level solution, $p_1 = p_2 = 3$, $(n_1 + 1) \times (n_2 + 1) = 64 \times 8$, $\overline{\varpi} = 10.0633$ Hz.

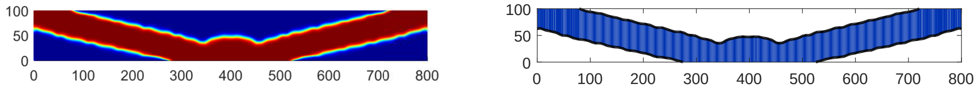

(i) Density map, $p_1 = p_2 = 3$, $(n_1 + 1) \times (n_2 + 1) = 80 \times 10$, $\overline{\varpi} = 9.76615$ Hz.

(j) Iso-level solution, $p_1 = p_2 = 3$, $(n_1 + 1) \times (n_2 + 1) = 80 \times 10$, $\overline{\varpi} = 10.0527$ Hz.

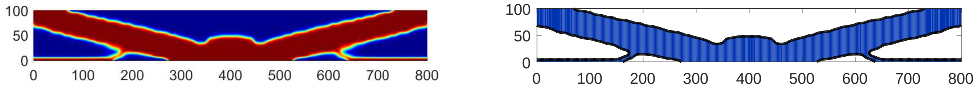

(k) Density map, $p_1 = p_2 = 3$, $(n_1 + 1) \times (n_2 + 1) = 96 \times 12$, $\overline{\varpi} = 9.7374$ Hz.

(l) Iso-level solution, $p_1 = p_2 = 3$, $(n_1 + 1) \times (n_2 + 1) = 96 \times 12$, $\overline{\varpi} = 10.0388$ Hz.

Figure B.6: NURBS solutions of P3.

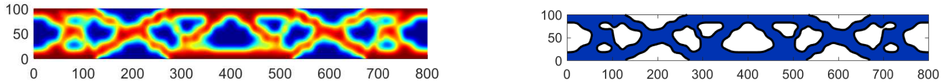

(a) Density map, $p_1 = p_2 = 2$, $(n_1+1) \times (n_2+1) = 64 \times 8$, $c_{dyn} = 4.8948$ Nmm.

(b) Iso-level solution, $p_1 = p_2 = 2$, $(n_1+1) \times (n_2+1) = 64 \times 8$, $c_{dyn} = 3.5396$ Nmm.

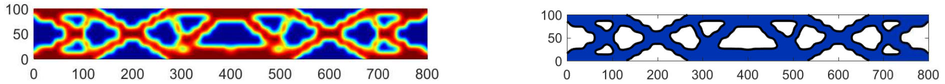

(c) Density map, $p_1 = p_2 = 2$, $(n_1+1) \times (n_2+1) = 80 \times 10$, $c_{dyn} = 4.4921$ Nmm.

(d) Iso-level solution, $p_1 = p_2 = 2$, $(n_1+1) \times (n_2+1) = 80 \times 10$, $c_{dyn} = 3.5336$ Nmm.

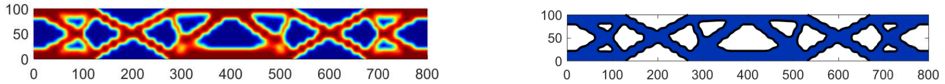

(e) Density map, $p_1 = p_2 = 2$, $(n_1+1) \times (n_2+1) = 96 \times 12$, $c_{dyn} = 4.2427$ Nmm.

(f) Iso-level solution, $p_1 = p_2 = 2$, $(n_1+1) \times (n_2+1) = 96 \times 12$, $c_{dyn} = 3.4876$ Nmm.

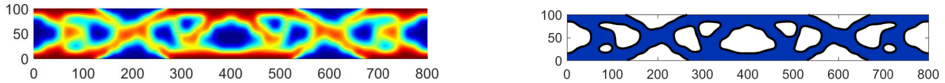

(g) Density map, $p_1 = p_2 = 3$, $(n_1+1) \times (n_2+1) = 64 \times 8$, $c_{dyn} = 5.1502$ Nmm.

(h) Iso-level solution, $p_1 = p_2 = 3$, $(n_1+1) \times (n_2+1) = 64 \times 8$, $c_{dyn} = 5.1743$ Nmm.

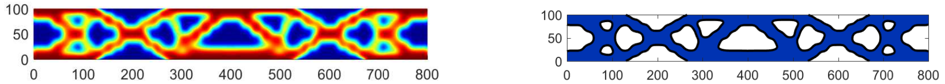

(i) Density map, $p_1 = p_2 = 3$, $(n_1+1) \times (n_2+1) = 80 \times 10$, $c_{dyn} = 4.7506$ Nmm.

(j) Iso-level solution, $p_1 = p_2 = 3$, $(n_1+1) \times (n_2+1) = 80 \times 10$, $c_{dyn} = 3.5725$ Nmm.

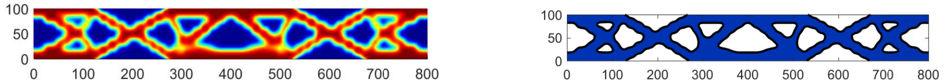

(k) Density map, $p_1 = p_2 = 3$, $(n_1+1) \times (n_2+1) = 96 \times 12$, $c_{dyn} = 4.4555$ Nmm.

(l) Iso-level solution, $p_1 = p_2 = 3$, $(n_1+1) \times (n_2+1) = 96 \times 12$, $c_{dyn} = 3.4717$ Nmm.

Figure B.7: B-Spline solutions of P4.

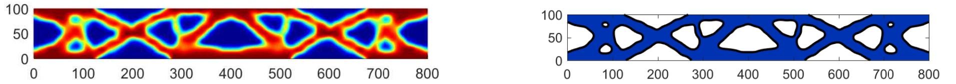

(a) Density map, $p_1 = p_2 = 2$, $(n_1+1) \times (n_2+1) = 64 \times 8$, $c_{dyn} = 4.4440$ Nmm.

(b) Iso-level solution, $p_1 = p_2 = 2$, $(n_1+1) \times (n_2+1) = 64 \times 8$, $c_{dyn} = 3.9313$ Nmm.

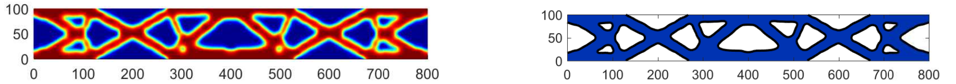

(c) Density map, $p_1 = p_2 = 2$, $(n_1+1) \times (n_2+1) = 80 \times 10$, $c_{dyn} = 4.1928$ Nmm.

(d) Iso-level solution, $p_1 = p_2 = 2$, $(n_1+1) \times (n_2+1) = 80 \times 10$, $c_{dyn} = 3.4658$ Nmm.

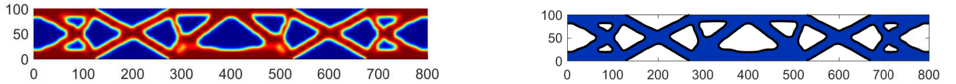

(e) Density map, $p_1 = p_2 = 2$, $(n_1+1) \times (n_2+1) = 96 \times 12$, $c_{dyn} = 4.0228$ Nmm.

(f) Iso-level solution, $p_1 = p_2 = 2$, $(n_1+1) \times (n_2+1) = 96 \times 12$, $c_{dyn} = 3.4572$ Nmm.

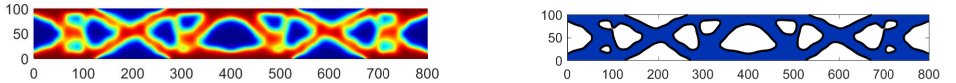

(g) Density map, $p_1 = p_2 = 3$, $(n_1+1) \times (n_2+1) = 64 \times 8$, $c_{dyn} = 4.6973$ Nmm.

(h) Iso-level solution, $p_1 = p_2 = 3$, $(n_1+1) \times (n_2+1) = 64 \times 8$, $c_{dyn} = 3.9800$ Nmm.

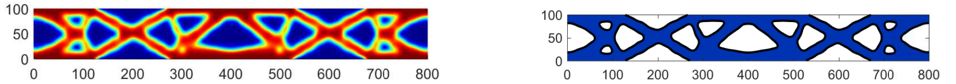

(i) Density map, $p_1 = p_2 = 3$, $(n_1+1) \times (n_2+1) = 80 \times 10$, $c_{dyn} = 4.4297$ Nmm.

(j) Iso-level solution, $p_1 = p_2 = 3$, $(n_1+1) \times (n_2+1) = 80 \times 10$, $c_{dyn} = 3.4842$ Nmm.

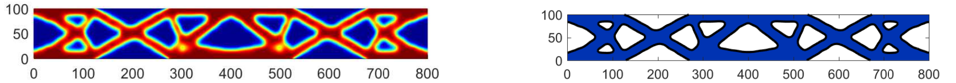

(k) Density map, $p_1 = p_2 = 3$, $(n_1+1) \times (n_2+1) = 96 \times 12$, $c_{dyn} = 4.2048$ Nmm.

(l) Iso-level solution, $p_1 = p_2 = 3$, $(n_1+1) \times (n_2+1) = 96 \times 12$, $c_{dyn} = 3.4592$ Nmm.

Figure B.8: NURBS solutions of P4.

References

[1] M. P. Bendsoe, N. Kikuchi, Generating optimal topologies in structural design using a homogenization method, Computer Methods in Applied Mechanics and Engineering 71 (2) (1988) 197–224. doi:https://doi.org/10.1016/0045-7825(88)90086-2.

[2] M. Bendsoe, O. Sigmund, Topology Optimization - Theory, Methods and Applications, Springer, 2003.

[3] J. A. Sethian, Level Set Methods and Fast Marching Methods - Evolving interfaces in computational geometry, fluid mechanics, computer vision, and materials science, Cambridge University Press, 1999.

[4] G. Allaire, F. Jouve, A.-M. Toader, Structural optimization using sensitivity analysis and a level-set method, Journal of Computational Physics 194 (1) (2004) 363 – 393. doi:https://doi.org/10.1016/j.jcp.2003.09.032.

[5] Y. Xie, G. Steven, A simple evolutionary procedure for structural optimization, Computers & Structures 49 (5) (1993) 885 – 896. doi:https://doi.org/10.1016/0045-7949(93)90035-C.

[6] J. Zhu, T. Gao, W. Zhang, Topology Optimization in Engineering Structure Design, Elsevier Science, 2016.

[7] W. Wittrick, Rates of change of eigenvalues, with reference to buckling and vibration problems, Journal of the Royal Aeronautical Society 66 (1962) 590 – 591. doi:https://doi.org/10.1017/S0368393100077385.

[8] Z.-D. Ma, H.-C. Cheng, N. Kikuchi, Structural design for obtaining desired eigenfrequencies by using the topology and shape optimization method, Computing Systems in Engineering 5 (1) (1994) 77 – 89. doi:https://doi.org/10.1016/0956-0521(94)90039-6.

[9] M. P. Bendsoe, N. Olhoff, J. E. Taylor, A variational formulation for multicriteria structural optimization, Journal of Structural Mechanics 11 (4) (1983) 523 – 544. doi:https://doi.org/10.1080/03601218308907456.

[10] I. Kosaka, C. C. Swan, A symmetry reduction method for continuum structural topology optimization, Computers & Structures 70 (1) (1999) 47 – 61. doi:https://doi.org/10.1016/S0045-7949(98)00158-8.

[11] A. P. Seyranian, E. Lund, N. Olhoff, Multiple eigenvalues in structural optimization problems, Structural optimization 8 (1994) 207 – 227. doi:https://doi.org/10.1007/BF01742705.

[12] J. Du, N. Olhoff, Topological design of freely vibrating continuum structures for maximum values of simple and multiple eigenfrequencies and frequency gaps, Structural and Multidisciplinary Optimization 34 (2) (2007) 91–110. doi:10.1007/s00158-007-0101-y.

[13] T. D. Tsai, C. C. Cheng, Structural design for desired eigenfrequencies and mode shapes using topology optimization, Structural and Multidisciplinary Optimization 47 (5) (2013) 673–686. doi:10.1007/s00158-012-0840-2.

[14] L. T. H., I. Hagiwara, Eigenfrequency maximization of plates by optimization of topology using homogenization and mathematical programming, JSME international journal. Ser. C, Dynamics, control, robotics, design and manufacturing 37 (4) (1994) 667–677. doi:10.1299/jsmec1993.37.667.

[15] N. Pedersen, Maximization of eigenvalues using topology optimization, Structural and Multidisciplinary Optimization 20 (1) (2000) 2–11. doi:10.1007/s001580050130.

[16] B. Niu, J. Yan, G. Cheng, Optimum structure with homogeneous optimum cellular material for maximum fundamental frequency, Structural and Multidisciplinary Optimization 39 (2) (2008) 115. doi:10.1007/s00158-008-0334-4.

[17] Z. Li, T. Shi, Q. Xia, Eliminate localized eigenmodes in level set based topology optimization for the maximization of the first eigenfrequency of vibration, Advances in Engineering Software 107 (2017) 59 – 70. doi:https://doi.org/10.1016/j.advengsoft.2016.12.001.

[18] D. Tcherniak, Topology optimization of resonating structures using simp method, International Journal for Numerical Methods in Engineering 54 (11) (2002) 1605–1622. doi:10.1002/nme.484.

[19] B. Niu, X. He, Y. Shan, R. Yang, On objective functions of minimizing the vibration response of continuum structures subjected to external harmonic excitation, Structural and Multidisciplinary Optimization 57 (2018) 2291 – 2307. doi:https://doi.org/10.1007/s00158-017-1859-1.

[20] C. JOG, Topology design of structures subjected to periodic loading, Journal of Sound and Vibration 253 (3) (2002) 687 – 709. doi:https://doi.org/10.1006/jsvi.2001.4075.

[21] H. Guan, Y.-J. Chen, Y.-C. Loo, Y.-M. Xie, G. P. Steven, Bridge topology optimisation with stress, displacement and frequency constraints, Computers & Structures 81 (3) (2003) 131 – 145. doi:https://doi.org/10.1016/S0045-7949(02)00440-6.

[22] O. S. J. S. Jensen, Systematic design of phononic band-gap materials and structures by topology optimization, Philosophical Transactions of the Royal Society of London. Series A: Mathematical, Physical and Engineering Sciences 361 (1806) (2003) 1001–1019.

[23] S. Min, S. Nishiwaki, N. Kikuchi, Unified topology design of static and vibrating structures using multiobjective optimization, Computers & Structures 75 (1) (2000) 93 – 116. doi:https://doi.org/10.1016/S0045-7949(99)00055-3.

[24] M. Alfouneh, L. Tong, Maximizing modal damping in layered structures via multi-objective topology optimization, Engineering Structures 132 (2017) 637 – 647. doi:https://doi.org/10.1016/j.engstruct.2016.11.058.

[25] G. Sun, D. Tan, X. Lv, X. Yan, Q. Li, X. Huang, Multi-objective topology optimization of a vehicle door using multiple material tailor-welded blank (twb) technology, Advances in Engineering Software 124 (2018) 1 – 9. doi:https://doi.org/10.1016/j.advengsoft.2018.06.014.

[26] J. S. Jensen, N. L. Pedersen, On maximal eigenfrequency separation in two-material structures: the 1d and 2d scalar cases, Journal of Sound and Vibration 289 (4) (2006) 967 – 986. doi:https://doi.org/10.1016/j.jsv.2005.03.028.

[27] W. Su, S. Liu, Topology design for maximization of fundamental frequency of couple-stress continuum, Structural and Multidisciplinary Optimization 53 (3) (2016) 395–408. doi:10.1007/s00158-015-1316-y.

[28] G. H. Yoon, Maximizing the fundamental eigenfrequency of geometrically nonlinear structures by topology optimization based on element connectivity parameterization, Computers & Structures 88 (1) (2010) 120 – 133. doi:https://doi.org/10.1016/j.compstruc.2009.07.006.

[29] J. Y. Noh, G. H. Yoon, Topology optimization of piezoelectric energy harvesting devices considering static and harmonic dynamic loads, Advances in Engineering Software 53 (2012) 45 – 60. doi:https://doi.org/10.1016/j.advengsoft.2012.07.008.

[30] A. Suksuwan, S. M. Spence, Performance-based multi-hazard topology optimization of wind and seismically excited structural systems, Engineering Structures 172 (2018) 573 – 588. doi:https://doi.org/10.1016/j.engstruct.2018.06.039.

[31] S. Allahdadian, B. Boroomand, Topology optimization of planar frames under seismic loads induced by actual and artificial earthquake records, Engineering Structures 115 (2016) 140 – 154. doi:https://doi.org/10.1016/j.engstruct.2016.02.022.

[32] L. Shu, M. Y. Wang, Z. Ma, Level set based topology optimization of vibrating structures for coupled acoustic–structural dynamics, Computers & Structures 132 (2014) 34 – 42. doi:https://doi.org/10.1016/j.compstruc.2013.10.019.

[33] J. A. Cottrell, T. J. Hughes, Y. Bazilevs, Isogeometric analysis: toward integration of CAD and FEA, John Wiley & Sons, 2009.

[34] L. Piegl, W. Tiller, The NURBS book, Springer-Verlag, Berlin, Heidelberg, New York, 1997.

[35] Y. Wang, Z. P. Wang, Z. Xia, L. H. Poh, Structural design optimization using isogeometric analysis: a comprehensive review, Comput. Model. Eng. Sci 109 (3) (1993) 455 – 507. doi:http://dx.doi.org/10.31614/cmes.2018.04603.

[36] X. Xie, S. Wang, M. Xu, Y. Wang, A new isogeometric topology optimization using moving morphable components based on r-functions and collocation schemes, Computer Methods in Applied Mechanics and Engineering 339 (2018) 61 – 90. doi:https://doi.org/10.1016/j.cma.2018.04.048.

[37] M. Xu, S. Wang, X. Xie, Level set-based isogeometric topology optimization for maximizing fundamental eigenfrequency, Front. Mech. Eng. 14 (2019) 222–234. doi:doi:10.1007/s11465-019-0534-1.

[38] L. Yin, F. Zhang, X. Deng, P. Wu, H. Zeng, M. Liu, Isogeometric bidirectional evolutionary structural optimization, IEEE Access 7 (2019) 91134–91145. doi:10.1109/ACCESS.2019.2927820.

[39] G. Costa, M. Montemurro, J. Pailhès, A NURBS-based topology optimization method including additive manufacturing constraints, in: 7th International Conference on Mechanics and Materials in Design, JF Silva Gomes and Shaker A. Meguid editors, 2017, p. 63.

[40] G. Costa, M. Montemurro, J. Pailhès, A 2D topology optimisation algorithm in NURBS framework with geometric constraints, International Journal of Mechanics and Materials in Design 14 (4) (2018) 669–696.

[41] G. Costa, M. Montemurro, J. Pailhès, NURBS hyper-surfaces for 3D topology optimization problems, Mechanics of Advanced Materials and Structures (2019) 1–20,doi:10.1080/15376494.2019.1582826.

[42] T. Rodriguez, M. Montemurro, P. L. Texier, J. Pailhès, Structural Displacement Requirement in a Topology Optimization Algorithm Based on Isogeometric Entities, Journal of Optimization Theory and Applications 184 (2020) 250 – 276.

[43] G. Costa, M. Montemurro, J. Pailhès, N. Perry, Maximum length scale requirement in a topology optimisation method based on NURBS hyper-surfaces, CIRP Annals 68 (1) (2019) 153 – 156.

[44] G. Costa, M. Montemurro, J. Pailhès, Minimum length scale control in a NURBS-based SIMP method, Computer Methods in Applied Mechanics and Engineering 354 (2019) 963 – 989.

[45] P. Bézier, Courbes et surfaces, Springer-Verlag, Paris: Hermès, 1986.

[46] C. de Boor, A practical guide to splines, Springer-Verlag, New York, 1978.

[47] G. Farin, Curves and Surfaces for CAGD: A Practical Guide, 5th Edition, Morgan Kaufmann Publishers Inc., San Francisco, CA, USA, 2002.

[48] N. Olhoff, J. Du, Generalized incremental frequency method for topological designof continuum structures for minimum dynamic compliance subject to forced vibration at a prescribed low or high value of the excitation frequency, Structural and Multidisciplinary Optimization 54 (2016) 1113 – 1141. doi:https://doi.org/10.1007/s00158-016-1574-3.

[49] J. Nocedal, S. J. Wright, Numerical Optimization, 2nd Edition, Springer Verlag, 2006.

[50] MathWorks, Inc, Optimization Toolbox User•̀s Guide Ralease 2017a, Natick, Massachusetts, United States, 2017.

[51] X. Gu, S.-T. Yau, Global Conformal Surface Parameterization, in: L. Kobbelt, P. Schroeder, H. Hoppe (Eds.), Eurographics Symposium on Geometry Processing, The Eurographics Association, 2003. doi:10.2312/SGP/SGP03/127-137.

[52] M. S. Floater, Parametrization and smooth approximation of surface triangulations, Computer Aided Geometric Design 14 (3) (1997) 231 – 250. doi:https://doi.org/10.1016/S0167-8396(96)00031-3.

[53] G. Bertolino, G. Costa, M. Montemurro, N. Perry, F. Pourroy, A general surface reconstruction method for post-processing of topology optimisation results, in: E. T. Conference (Ed.), 2nd International Conference on Simulation for Additive Manufacturing, The Eurographics Association, 2019.